CHALMERS

Event Generator for R^{3}B

Master Thesis in Physics and Astronomy

STEFAN BULLER

Department of Fundamental Physics
CHALMERS UNIVERSITY OF TECHNOLOGY
Gothenburg, Sweden 2015

Event Generator for R^{3}B

Master's Thesis

by

Stefan Buller

Supervisors:

Andreas Heinz

Examiners:

??

Department of Fundamental Physics
Chalmers University of Technology
Gothenburg, Sweden 2015

Cover: The prefered decay modes for various nuclei at an excitation energy of 15 MeV, according to the code developed in this project. A red box signifies that the nucleus preferentially decays by emitting a proton, while a blue box means that neutron emission is the most common decay mode. Cyan boxes corresponds to nuclei who deexcite primarily by emitting an alpha particle.

Abstract

This thesis describes...

Acknowledgements

Contents

1. Introduction

As a part of the construction of the international FAIR (Facility for Antiproton and Ion Research), the LAND experimental setup will be succeeded by the R^{3}B (Reactions with Relativistic Radioactive Beams) setup, which includes a score of new detectors. During all stages of this process – from designing and calibrating the new individual detectors and the entire setup, to analyzing the data and extracting the underlying physics – simulations are or will be used.

The R^{3}B experiment aims to study nuclear physics, in particular the properties of exotic nuclei far from the valley of stability [1]. The experiments will be performed with radioactive beams, and the aim is to be able to determine the complete kinematics of the reaction. We will here describe a generic experiment of this kind.

The radioactive beam impinges on a target surrounded by detectors. In the case of a reaction at the target – a so called *event* – the reaction products are to be indeitifed by the experimental setup. This is done by recording where they hit the detector, when they hit the detectors (which allows detector output to be attributed to individual events, which yields the initial and final momentum); how much energy they deposit in the detectors (yielding the charge); and their deflection in a magnetic field, which gives their charge-to-mass ratio, and thus their mass.

That being said, the identification procedure outlined above is a simplification. Complications arise from several factors: the reaction products may decay in-flight, they may be deflected by interactions with air, or a detector. This is why simulations are used, specifically Monte-Carlo simulations, since the underlying physics is non-deterministic.

While simulations are used to study how a given reaction product propagates throughout the experimental setup, they are not necesarilly needed for the actual reactions at the target, since the purpose of the experiment is to investigate those. In many cases, it is enough to simulate particles with specified initial momenta – matching the kinematic constraints of the reaction – and see how they propagate through the experimental setup, which should be able to identify them even if they are not the result of an actual reaction. However, since the setup should in practice identify only actual reactions products, it would be more efficient if the simulations incorporated some of the theory on the reactions to be studied.

Having complete knowledge of the outgoing particle in the simulation may also tempt the user to overestimate the detector efficiency, since they will more easily be able to identify their particle when they know what they are looking for, given that no other

processes are involved.

1.1. Event Generator for R^{3}B

As briefly mentioned in the previous section, an experimental event is the result of a reaction between the target and a projectile. An *event generator*, on the other hand, is in this context a code that mimics certain reactions as part of a larger simulation code. The output of such an event generator would be final state momenta and energies of the reacting particles, which can then be propagated through the simulated experimental setup by another code.

In principle, one can think of an event generator that exactly simulates the reactions at the target and returns a final state with a probability mimicing the experiment. However, there are good reasons not to implement this event generator, not all of them related to how unfeasible that project would be, considering our present knowledge of nuclear physics. This will be discussed in the following section.

1.1.1. Design of an Event Generator

An event generator for R^{3}B needs to have certain features: Firstly, it does not need to reproduce every feature of the experimental spectra, as long as it reproduces the general features. The actual experiment will determine the details. On the other hand, it needs to be easy to change the underlying model and see how this influences the resulting spectra, since quantities in the model – nuclear level densities, transition rates, etc. – are influenced by the presence of phenomena the experimenters are actually interested in finding – such as giant resonances or halo structures – which are not directly observable in the experimental data.

It is also desirable to be able to steer the event generator to generate specific kinds of events, so that the efficiency of the experimental setup can evaluated for specific reactions.

The software also needs to be suitable for use with other programs in use in the R^{3}B collaboration. These programs are presented in the next section.

1.2. Already existing software

The event generator is intended to be used together with GEANT4, which is a widely used toolkit for simulating the interaction of particles in matter [2]. It takes advantage of the wrapper program GGLAND [3] – which is designed to make it easy to run the simulations needed for the analysis of the LAND/R^{3}B experiments – to tell with GEANT4 which particles to simulate and how the experiment is set up.

In addition to the software the event generator is intended to work with, there are a few codes which have been helpful during the development process:

The code is largely based upon CODEX [4], which simulates fusion and the subsequent decay of a compound nucleus. The choice of models in this work is largely based on

a setting in CODEX. The quasi-elastic scattering part of the code (described in subsection 2.1.1) has been adapted from the QUASI_ELASTIC code, written by Leonid Chulkov.

Finally, part of the output of the event generator was compared to that of an already existing code, TALYS [5].

2. Theoretical Background

In the following section, the theoretical models implemented in the event generator code are presented. We use units in which $c = 1$, which means that mass, momentum and energy are given in the same units, customary taken to be *electron-volt*, or, for the energies of interest in nuclear physics, MeV or GeV. We do not set $\hbar$ to one.

2.1. Nuclear Collisions

From a macroscopic perspective, nuclei can be viewed as charged particles, and thus collisions (here in a loose sense) between them are governed by the Rutherford scattering formula. This is how the nucleus was discovered in the first place. However, this simple picture breaks down at higher energies, when the particles are able to cross the Coulomb barrier. At yet higher energies, when the de Broglie wave-length ($\lambda \sim \boldsymbol{p}^{-1}$) becomes sufficiently small to resolve the inner structure of the nuclei, it becomes feasible to model the collision as not taking place between the two nuclei, but by individual protons and neutrons (nucleons).

This leads us to the *participant-spectator* picture of nuclear collisions, in which the collision is viewed as if taking place between a few *participant* nucleons, while the remaining *spectator* nucleons remain mostly unaffected. Such a reaction is known as *quasi-elastic scattering*, since the kinetic energy of the projectile is much greater than the binding energy of the participants, which further motivates treating them as approximately free particles. This also means that the kinetic energy will almost be conserved, hence *quasi-elastic*. The collision between the participant nucleons takes place at a time scale of about 10^{-23} s [6], and is sometimes called a *fireball* or *firestreak*.

However, this is just the first part of the collision. The spectator nucleons may have gone unaffected through it, but the resulting system (a so-called pre-fragment) will be highly excited, and will decay to the final fragment – often by ejecting nucleons, in this context known as evaporating them. The characteristic time-scale for these ejections varies between 10^{-21} – 10^{-16} s, depending on the energies and emitted particle [6].

In this picture, a two-step process can be used to describe nuclear fragmentation. Various models to describe both steps exist in the literature, and these can be combined more or less freely – restrictions arise since they do not necesarilly use the same parameters. Models which mainly use parameters like A, the number of nucleons, Z the number of protons, the total nuclear-spin J and the excitation energy E of the nucleus
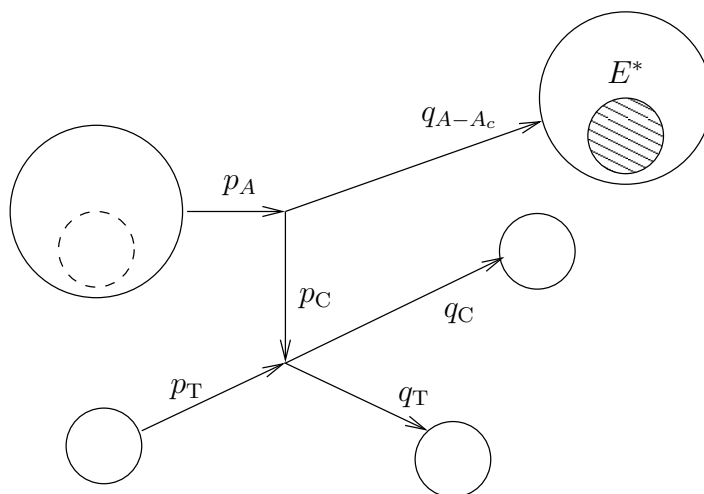
Figure 2.1.: *The fast process. The projectile (A) is viewed as a system of a cluster and prefragment. The collision then takes place between the cluster and the target.*

are termed *macroscopic*, while models that directly treat the states of individual nucleons are called *microscopic*. Examples of the former are the *abrasion-ablation model* [7], while the *intranuclear-cascade model* [8] is an example of a microscopic model. As it is often the case in nuclear physics, no one model is valid for the whole range of nucleon numbers A and incident energies [9].

Since the focus of this report is to describe an event-generator for a physics experiment, we can afford to use less detailed models if this reduces computation time. In addition, since the macroscopic properties of nuclei are more easily related to expermental observables, we will restrict our attention to those.

2.1.1. The fast processes – the Goldhaber model

In the participant-spectator picture, the fast process consists of a collision between the target and a cluster within the projectile nucleus. This is determined by momentum conservation, but in order to apply this, we need to know the initial momentum of the internal cluster, which will have a momentum relative to the projectile. The situation is illustrated in Figure 2.1.

The *Goldhaber model* states that the 3-momentum distribution is given by a Guassian with the width determined by the expectation value of the momentum of an individual nucleon, explicitly

$$\sigma^2 = \langle \boldsymbol{p}_{\text{nucleons}}^2 \rangle A' \frac{A_{\text{C}}}{A - 1}, \tag{2.1}$$

where A is the number of nucleons in the projectile, $A' = A - A_{\text{cluster}}$ the nucleon number of the prefragment, and $\langle \boldsymbol{p}_{\text{nucleons}}^2 \rangle$ is the expectation value of the 3-momentum

of an individual nucleon. For a Fermi-gas, $\langle p^2 \rangle$ may be written in terms of the Fermi-momentum $\boldsymbol{p}_f$ as $\frac{3}{5}\boldsymbol{p}_f^2$ [10]. The nuclear Fermi-momentum, assuming a constant density, is about $270\,\text{MeV}$, which is in reasonable agreement with experiments for heavier ($A > 40$), non-exotic nuclei [11].

However, R^{3}B experiments are not necesarilly about heavy (and non-exotic) nuclei. Another model – also a "Goldhaber model", since it uses a Guassian momentum distribution – gives σ^2 as

$$\sigma^2 = 2(M_{A'} + M_\text{C} - M_A)\frac{M_\text{C}M_{A'}}{M_\text{C} + M_{A'}} = -2Q\mu(M_\text{C}, M_{A'}), \tag{2.2}$$

where M_C is the mass of the participant cluster, M_A the mass of the projectile and $M_{A'}$ the mass of the prefragment. If we take $-Q = T = \mu v^2/2$, we get $\sigma^2 = \mu^2 v^2$, which is the initial squared momentum of the cluster, provided that we can neglect the kinetic energy of A'. This model is suitable for lighter particles, since it requires that $M_{A'} + M_\text{C} - M_A = -Q > 0$, or σ^2 becomes negative. This is the model used in this work.

Momentum conservation implies that

$$p_A = p_\text{C} + q_{A'} \tag{2.3}$$
$$p_\text{C} + p_\text{T} = q_\text{C} + q_\text{T} \tag{2.4}$$

where the momenta are defined in Figure 2.1, with the additional definition of $A' = A - A_\text{C}$. The initial momentum of the cluster, p_C, in addition to being partly defined by the Goldhaber model, is also fully specified by the external momenta: viewing Figure 2.1 as a Feynman diagram even makes it clear that the cluster is *off-shell*. With this in mind, we solves the first of the above equation for p_C by squaring, which gives

$$M_{\text{C,off}}^2 \equiv p_\text{C}^2 = p_\text{A}^2 + q_{\text{A}'}^2 - 2p_\text{A}\cdot q_{\text{A}'} = M_\text{A}^2 + M_{\text{A}'}^2 - 2M_\text{A}\sqrt{M_{\text{A}'}^2 + \boldsymbol{p}_\text{C}^2}, \tag{2.5}$$

where we have evaluated $p_\text{A} \cdot q_{\text{A}'}$ in the rest-frame of the prefragment. Note that since the prefragment is excited $M_{\text{A}'}$ will have to be adjusted by adding the excitation energy.

Since we are interested in constructing an event generator, we next transform the 4-momentum of the cluster from the projectile to the laboratory frame (the projectile and target momentum are already known in the laboratory frame – the former being zero is practically the definition of that frame). The relevant gamma factor is $\gamma = 1 + T/M_A$, where T is the kinetic energy of the projectile.

Since the collision between the target and the cluster is easier to do in their center-of-mass (CM) frame[1], we also need to transform between the laboratory and that frame. This is readily done by noting

$$\bar{\boldsymbol{P}} \equiv \boldsymbol{p}_\text{C} + \boldsymbol{p}_\text{T} = \gamma(\beta_{\text{ZM}})\bar{m}\boldsymbol{\beta}_{\text{CM}} = \bar{E}\boldsymbol{\beta}_{\text{CM}} \implies \boldsymbol{\beta}_{\text{CM}} = (\boldsymbol{p}_\text{C} + \boldsymbol{p}_\text{T})/\bar{E}, \tag{2.6}$$

---

[1]Strictly speaking, their zero momentum frame, or center-of-momentum frame.

where the barred quantities are of the system of both particles. Since we want the β between the laboratory and the CM frame, we evaluate all the quantities in the laboratory frame

$$\boldsymbol{\beta}_{\mathrm{CM}} = \frac{\boldsymbol{p}_{\mathrm{C}}}{E_{\mathrm{C}} + M_{\mathrm{T}}}. \tag{2.7}$$

The scattering between target and cluster is back-to-back in the CM frame, and we generate the scattering angle from an isotropic $\frac{d\sigma}{dt}$, which in practice means that the Mandelstam variable $t = (p_{\mathrm{C}} - q_{\mathrm{C}})^2$ is a uniform random number. The CM energy, momentum and scattering angle can be readily expressed in terms of the invariant Mandelstam variables

$$E_{\mathrm{C}} = \frac{s + M_{\mathrm{C,off}} - M_{\mathrm{T}}}{2\sqrt{s}} \tag{2.8}$$

$$|\boldsymbol{p}_{\mathrm{C}}| = \sqrt{E_{\mathrm{C,initial}}^2 - M_{\mathrm{C,off}}^2} \tag{2.9}$$

$$|\boldsymbol{q}_{\mathrm{C}}| = \sqrt{E_{\mathrm{C,final}}^2 - M_{\mathrm{C}}^2} \approx |\boldsymbol{p}_{\mathrm{C}}| \tag{2.10}$$

$$\cos\theta \approx \frac{t - N_{\mathrm{C}}^2 - N_{\mathrm{C}}^2 + 2E_{\mathrm{C}}^2}{2|\boldsymbol{p}_{\mathrm{C}}|^2}, \tag{2.11}$$

the approximations being valid under the assumption of a quasi-elastic scattering, more explicitly when $M_{\mathrm{C,off}} \approx M_{\mathrm{C}}$, so that $\boldsymbol{p}_{\mathrm{C}} = -\boldsymbol{q}_{\mathrm{C}}$ in the CM frame, which is the assumption used in deriving the equation for $\cos\theta$.

A random polar angle ϕ in $[0,2\pi]$ is then generated, which together with $|\boldsymbol{p}_{\mathrm{c}}|$, θ and E_{c} fixes the CM 4-momentum of the cluster, and also the target by $\boldsymbol{p}_{\mathrm{t}} = -\boldsymbol{p}_{\mathrm{c}}$. Using (2.7), these results are boosted to the lab frame, in which we now have an expression for all the relevant momenta.

2.1.2. The slow process – decay of a compound nucleus

To describe the decay of a compound nucleus in a given macro-state (E^*, J, Z, A), we need the probabilities to go from this state to any other macro-state. Since the only way an isolated nuclei can lose energy, angular momentum, or nucleons is by emitting particles, it is natural to view the transition probability as in terms of quantities related to particle emission.

The formula used to describe this gives the probability of decaying by evaporating a particle ν as

$$\frac{d^2 P_\nu}{dE_f^* dt} = \frac{1}{\hbar} \frac{\rho(E_f^*, J_f)}{\rho(E_i^*, J_i)} \sum_{S=|J_f - s|}^{|J_f + s|} \sum_{l=|J_i - S|}^{|J_i + S|} T_l(\epsilon_\nu), \qquad [12] \tag{2.12}$$

where P is the probability, E_f^* the final-state excitation energy, J_f the final-state spin, ρ the level densities and

$$\epsilon_\nu \approx E_f^* - E_i^* - S_\nu \tag{2.13}$$

the kinetic energy of the evaporated particle, S_ν being its separation energy $S_\nu = M_f + m_\nu - M_i$[2]. Continueing: s is the intrinsic spin of the evaporated particle, S is the spin of the system consisting of the final state nucleus and evaporated particle, with l being the orbital angular momentum of that state with respect to its center of mass. The sums express all the ways to couple these angular momenta while conserving the total angular momentum $\boldsymbol{J}_f + \boldsymbol{s} + \boldsymbol{l} = \boldsymbol{S} + \boldsymbol{l} = \boldsymbol{J}_i$. Finally, T_l is the transition probability.

By integrating over E^*, we get $\hbar \frac{dP_\nu}{dt} = \Gamma_\nu$, which is proportional to the probability to decay via the channel ν, $P_\nu = \Gamma_\nu / \Gamma_{\text{tot}}$.

Provided that the characteristic life-time Γ_{tot}^{-1} of the system is short compared to the time resolution of the experimental setup, we may treat the decays as instantanous. Note that the system may undergo multiple decays before it reaches its ground-state, and that time-scale of this entire decay chain must be short by the experimental standards. The time-of-flight resolution of the future R^{3}B setup will be in the picosecond range (10^{-12} s) [1], which is well above the time-scales of single evaporation given by Gaimard and Schmidt (10^{-21} – 10^{-16} s) [6]. Hence we will view Γ_x as the probability to decay by a given process in an unspecified but short time step.

Since we are interested in simulating a decay chain, we want more information than merely the probability to decay by emitting a specific particle. We thus take a step back from (2.14), and undo the summation over l

$$\frac{d\Gamma_{\nu,l}}{dE_f} = \frac{\rho(E_f, J_f)}{\rho(E_i, J_i)} \sum_{S=|J_f-s|}^{|J_f+s|} T_l(\epsilon_\nu), \quad l \in \{|J_i - S|, ..., |J_i + S|\} \tag{2.14}$$

which finally gives us the decay probability (per unit energy) from an initial state (E_i, J_i) to a final state (E_f, J_f) by emmiting a particle ν with angular momentum l.

The emitted particle, ν, can in principle be anything a nucleus may decay by emitting. However, the photon must be treated differently as it is massless and thus fully relativistic – which makes the dististinction between l and the intrinsic spin unnatural – and removes a polarization state. With this in mind, we obtain

$$\frac{d\Gamma_\gamma}{dE_f} = \frac{\rho(E_f, J_f)}{\rho(E_i, J_i)} \sum_{l=|J_f-J_i|}^{|J_f+J_i|} T_l(\epsilon_\gamma) \tag{2.15}$$

$$\implies \frac{d\Gamma_{\gamma,l}}{dE_f} = \frac{\rho(E_f, J_f)}{\rho(E_i, J_i)} T_l(\epsilon_\gamma), \tag{2.16}$$

where $l > 0$ is an integer.

Although ν could be any particle, it becomes more appropriate to model the decay as a fission process if ν becomes sufficiently heavy in relation to the compound nucleus.

---

[2]The approximation is due to neglecting the kinetic energy of the daughter nucleus, which should be a good approximation when the evaporated particle ν is light. This is not a necesary approximation, though, and a more exact formula is $\frac{m_\nu}{\mu}\epsilon_\nu \approx E_f^* - E_i^* - S_\nu$. The separation energy does not enter as a cost of removing the particle ν, but rather to relate the two excitation energies E_f^* and E_i^* to an absolute scale.
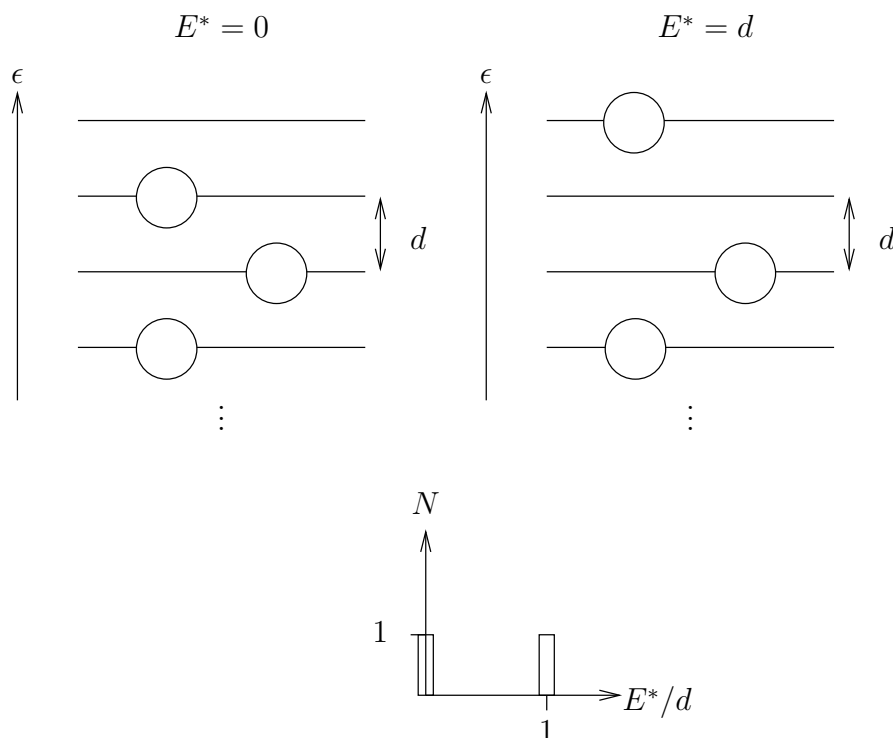
Figure 2.2.: *Fermions with equidistant single-particle levels.*

Fission is usual modeled as a transition first to a *transition state*, beyond which the nucleus will inevitably fission [13]. The present work does not include fission, and we will thus not discuss its details here. Swiateck discussed the possibility of treating particle emission and fission in an essentially symmetric fashion, by using a transition state formalism also for lighter particles [14].

We will now describe models for the level density ρ and transition probability T_l.

Level densities

The level density $\rho(E,J)$ enumerates the number of energy levels of a given nucleus in an energy range $[E,E + dE]$ with a given spin J. We have in our notation supressed the dependence on A and Z. The nuclear level density increases rapidly with energy, which suggests that the nuclear levels are not simply built up by exciting single nucleons, since the spacing of these levels do not decrease nearly fast enough.

To see how the rapid increase in level densities may be accounted for by collective excitations, and to introduce some of the terminology, it is illustrative to have a look at a simple example.

The simple example   Consider a "nucleus" in which we have A identical nucleons, that occupy single particle states with spacing d. The situation is illustrated in Fig-

ure 2.2. The energy of the nuclues is given by

$$E = \sum_{i}^{\infty} \epsilon_i n_i, \tag{2.17}$$

where $\epsilon = id$ is the energy of level i, and n_i is the occupation number of that level, which can be 0 or 1, since nucleons are fermions. If we take the Fermi energy as the reference energy, we get the excitation energy

$$E^* = \sum_{i}^{\infty} \epsilon_i n_i - \sum_{i}^{A} \epsilon_i. \tag{2.18}$$

The picture is more illustrative than the formulas. We now have one way to excite our system to $E^* = d$, namely by exciting the nucleon just below the Fermi level. For $E^* = 2d$ we may proceed from our $E^* = d$ system in two ways, either by further exciting the lone excited nucleon $E^* = 2d$, or by exciting the highest nucleon in the $A-1$ system, $E^* = d + d$. For $E^* = 3d$, we have

$$1d + 1d + 1d$$
$$2d + 1d \tag{2.19}$$
$$3d,$$

and at this point, it may be apparent that we are really investigating the number of ways to write a natural number as a sum of natural numbers, a problem which engaged Euler as early as 1720 [15]. It turns out to be a very rapidly growing function, with the number of ways to partition 100 being 190569292 [15].

A few things to note: Firstly, there is a distinction between the level density, discussed above, and the *density of states*. In our example above, we may imagine that each configuration of nuclei corresponds to a state with a given spin J, which would give us $(2J - 1)$ different spin projections for each state. The density of states takes this degeneracy into account, while the level density does not. The density of states is thus greater than the level density. Of course, we do not know the J of our states but there is a general argument for the J dependence of the level density. Following the derivation by Grossjean and Feldmeier [16] we assume that the states are build up from single-particle states with a random spin orientation. More precisely, let the single-particle states spin projection m be a random number. Time-reversal symmetry demands that the expectation value of m is zero, and that their distribution is symmetric. Now, if we assume that our state is formed by exciting a large number of nucleons, the central limit theorem gives the probability of the total spin projection M as

$$P(M) = \frac{1}{\sqrt{2\langle M^2\rangle}} \exp\left(-\frac{M^2}{2\langle M^2\rangle}\right), \tag{2.20}$$

and hence the density of states ω with spin-projection M specified becomes

$$\omega(E^*)_M = \frac{\omega(E^*)}{\sqrt{2\langle M^2\rangle}} \exp\left(-\frac{M^2}{2\langle M^2\rangle}\right). \tag{2.21}$$

Finally, using the fact that for each fixed J, say J', there is only one state of each $M \in [-J', \ldots, J']$, we may subtract contributions from all states with higher[3] J by:

$$\rho_{J'}(E^*) \equiv \omega(E^*)_{M=J',J=J'} = \omega(E^*)_{M=J'} - \omega(E^*)_{M=J'+1}, \tag{2.22}$$

where the equivalence is due to the fact that $\rho_J(E^*) = \omega(E^*)_{M,J}$ for any fixed value of M. For $J \ll \sqrt{\langle M^2 \rangle}$, this is approximated as

$$\rho_J(E^*) \approx -\frac{d}{dM} \left(\omega(E^*)_M\right)_{M=J+1/2}, \tag{2.23}$$

which gives the J dependence as

$$\rho_J(E^*) \approx \frac{\omega(E^*)}{\sqrt{2\langle M^2 \rangle}} \frac{2J+1}{2} \exp\left(-\frac{M^2}{2\langle (J+1/2)^2 \rangle}\right). \tag{2.24}$$

Secondly, for higher excitation energy, it makes sense to smear out the discrete levels in order to get a continous function – and get it on a closed form. The usual way this is done is by observing that the grand partition function

$$Z(\alpha,\beta) = \sum_{i,A} \rho(E,A) \exp\left(\alpha A - \beta E_i(A)\right) \tag{2.25}$$

formally is the Laplace-transform of the density of states, which gives us

$$\rho(E,X) = \frac{1}{2\pi i} \int_{-i\infty}^{i\infty} Z(E,X) \exp\left(\beta E - \alpha A\right). \tag{2.26}$$

The "smearing out" is now done by applying a saddle-point approximation to the above integral; see, for example, Goutis et. al. [17].

Having said this, we now present the expression for the level density used in this work:

$$\rho(E^*,J) = \frac{1}{\sqrt{2}\,24} \frac{1}{\sigma a^{1/4} U^{5/4}} \exp\left(2\sqrt{aU}\right) \frac{2J+1}{\Theta_{\text{eff}}/(\hbar^2\beta)} \, exp\left(-(J+\tfrac{1}{2})^2/(2\Theta_{\text{eff}}/(\hbar^2\beta))\right), \tag{2.27}$$

which is a version of the widely-used expression for the level density of a *Fermi gas* that takes angular momentum J into account, in accordance with the theory presented above [18].

Here, U is an effective excitation energy above the *yrast line*, corrected for shell and pairing effects. It is given by

$$U = E_{\text{eff}} + f(E_{\text{eff}})\delta S + g(E_{\text{eff}})\delta P, \tag{2.28}$$

where f and g describe the damping of shell and pairing effects with increasing energy, and $E_{\text{eff}} = E^* - E_{\text{yrast}}$. The *yrast energy*[4], E_{yrast}, is the lowest energy for a given angular momentum, here taken to be

$$E_{\text{yrast}} = \frac{J(J+1)\hbar^2}{2\Theta_\perp}, \tag{2.29}$$

---

[3]states with lower J, $J < J'$, do not contribute, since they do not contain a $M = J'$ state.

[4]From the Swedish word "yrast", which in this context means "whirliest" [19].

which is the energy corresponding to a quantum-mechanical axial-symmetric rotor rotating around a symmetry axis perpendicular to its elongation. This yrast energy is not, strictly speaking, the lowest energy for a given J, but the energy of a collective rotational excitation [20]. As may be interfered by comparing (2.24) with (2.27), the expectation value $\langle M^2 \rangle$ is closely connected to the moment of inertia Θ. Ericson [20] provides a simple, although not especially rigirous, explanation for this: If we assume that a nucleus of spin J has some of its energy in a rotational excitation of the form expected of a classical rotor, $\frac{\hbar^2 J^2}{2\Theta}$, then it will not have this energy available for intrinsic excitations[5]. Hence, we adjust the energy according to $E^* \rightarrow E^* - \frac{\hbar^2 J^2}{2\Theta}$, as we have done above in the effective excitation energy (2.28). Furthermore, if we approximate the rapidly growing $\rho(E^*)$ as an exponential, we can write

$$\rho(E^* - \frac{\hbar^2 J^2}{2\Theta}) = \rho(E^*) \exp\left(\frac{\hbar^2 J^2}{2\Theta}\right), \tag{2.30}$$

and comparing this equation with (2.24) gives a direct relation between Θ and $\langle M^2 \rangle$. We now return to Equation 2.28.

Shell and pairing energy   The pairing energy δP can be estimated from the average separation energy for the surrounding nuclei (in an (N,Z) plot, like an isotope chart), which is close to the actual observed shift between odd and even nuclei [20]. Neutrons and protons have different pairing energies, which is to be added or subtracted when neutron or proton number, respectively, is odd or even. The shell energy δS can either be calculated from a microscopic model, or – as I have done – can be be estimated together with the pairing energy by comparing experimental masses with masses predicted by a macroscopic model, and taking the difference, as suggested by Schmidt and Morawek [12]. I used the macroscopic part of the 1992 edition of the Finite-Range Droplet Model (FRDM-1992) [21], which is presented in more detail in section 2.2.

The damping of shell effects with energy can be described by an exponential function

$$f(E_{\text{eff}}) = 1 - \exp\left(-E_{\text{eff}}/E_{\text{d}}\right), \tag{2.31}$$

where E_{d} is the shell-damping energy

$$E_{\text{d}} = \frac{0.4}{a} A^{4/3}, \tag{2.32}$$

where a is the level-density parameter, which for a spherical nuclei can be approximated by

$$a = \frac{A}{14.61\,\text{MeV}}(1 + 3.114 A^{-1/3} + 5.626 A^{-2/3}). \qquad [12] \tag{2.33}$$

This parameter also enters directly into (2.27), and is directly related to the inverse level spacing at the Fermi level, $a = \frac{\pi^2}{3}\frac{1}{d}$.

---

[5]The $\hbar$ being there to compensate for the fact that J is dimensionless in our notation.

Likewise, the damping of pairing effects with energy can also be described by a simple function, in this case

$$g(E_{\text{eff}}) = \begin{cases} 1 - (1 - E/E_{\text{c}})^2 & E_{\text{eff}} < E_{\text{c}} \\ 1 & E_{\text{eff}} \geq E_{\text{c}}. \qquad [12] \end{cases} \tag{2.34}$$

The critical energy E_{c} is approximately $10\,\text{MeV}$ and is taken to vary with angular momentum,

$$E_{\text{c}} = 10\,\text{MeV}\sqrt{1 - (J/J_{\text{c}})^2}, \tag{2.35}$$

where the critical angular momentum J_{c} has been set to $12\hbar$[6].

Moment of inertia Since we have restricted ourselves to spherical nuclei in (2.33), we also have the moments of inertia $\Theta_{\perp} = \Theta_{\parallel}$. In particular, for a sphere with constant density, we have

$$\Theta = \frac{2}{5}MR_0^2 \approx \frac{2}{5}A^{5/3} \times u \times r_0^2 \tag{2.36}$$

The approximation is obtained by inserting $R_0 = r_0 A^{1/3}$ and $M = uA$, where $r_0 = 1.16\,\text{fm}$ is the nuclear radius constant, with the same value as in the macroscopic model [21]. u is the atomic mass units, $u \approx 931.5\,\text{MeV}$.

Reciprocal tempeture β Finally, β in (2.27) is the reciprocal nuclear temperature[7] $\beta = 1/T$. It can be calculated from $\frac{a}{\beta}$, which is obtained by solving

$$a/\beta = \sqrt{(aU)[1 - exp-a/\beta]}, \qquad [16] \tag{2.37}$$

which can be done numerically by iterating

$$(a/\beta)_{n+1} = \sqrt{aU[1 - exp-(a/\beta)_n]} \tag{2.38}$$

from a suitable initial guess $(a/\beta)_0$. $(a/\beta)_0 = \sqrt{aU}$ was used here, which solves (2.37) for $(a/\beta) \to \infty$ and is known to be a good initial guess [16].

The level density of ^{20}Ne for different spin with and without subtracting the yrast-energy is illustrated in Figure 2.3. As can be seen in the figure, the level densities for higher spin start at a lower value for low energies, way lower than $1\,\text{level/MeV}$, which indicates that the continous view of energy levels fails at these energies. The spins appear to be split up in 2 groups, one for $J \leq 1$ and one for $J > 1$. The level densities for $4 \geq J > 1$ initially grow rapidly, until they overtake the lower spin level densities and settle at a seemingly proportional relationship with each other. As a result of the $(2J + 1)\exp\left(-(J + 1/2)^2\right)$ dependence on J, moderate J values give the largest level density. The same general behaviour is seen for the other nuclei at the $A = 20$ isobar.

---

[6]The value of the critical angular momentum and the momentum dependence in general is from the CODEX code. I have not been able to find any other source.

[7]It really is the reciprocal temperature at the saddle-point, see e.g. Feldmeier [16].

(a) The level densities derived from (2.27).

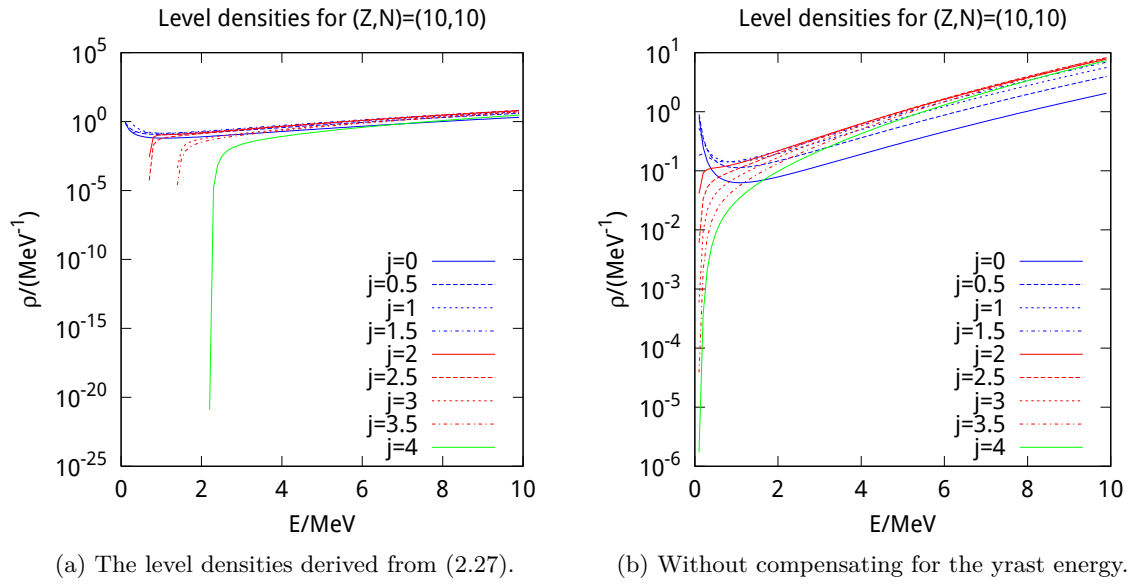(b) Without compensating for the yrast energy.

Figure 2.3.:   *The energy dependence of the level density of ^{20}Ne for spin $J = 0, \frac{1}{2}, \dots, 4$. In order to be able to compare level densities for different spin at the same effective energy above the yrast line, the yrast energy has not been subtracted from E_{eff} in 2.3b.*
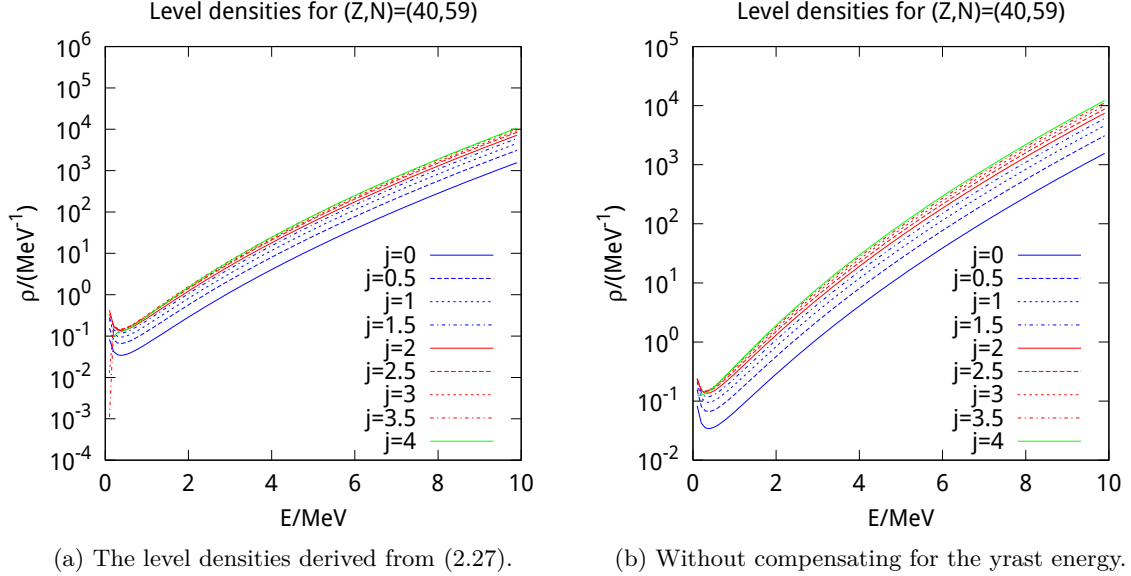
(a) The level densities derived from (2.27).

(b) Without compensating for the yrast energy.

Figure 2.4.: *The energy dependence of the level density of ^{99}Zr for spin $J = 0, \frac{1}{2}, \ldots, 4$. In order to be able to compare level densities for different spin at the same effective energy above the yrast line, the yrast energy has not been subtracted from E_{eff} in 2.4b.*

In order to see if this is a general feature of our model, we also investigate ^{99}Zr – this nucleus is being chosen arbitrarily as an example of a non-fissile nucleus far form the $A = 20$ isobar. The corresponding plots of the level densities are seen in Figure 2.4. We note that the inclusion of the yrast energy is not nearly as significant for the spins under consideration, since the larger value of Θ reduces the yrast energy of a given J. This also explains why $J = 4$ has the highest density of states in this case: a higher Θ means that the $\exp\left(-(J + 1/2)^2/\Theta\right)$ factor does not supress the level density as rapidly with increasing spin. We also see that it is only for $J \geq 3$ that we see the hint of a dip for lower energies. This could perhaps indicate that the pronounced spin-dependence seen for the $A = 20$ isobar will reveal itself for yet higher spin – a natural consequence of the higher moment of inertia for heavier nuclei.

In any case, this is low-energy behaviour, and both the Fermi gas model [16] and the very notion of a continuous level density has problems for low energies. Most notably, the Fermi gas model itself, without compensating for shell and pairing effects, predicts a singularity at $U = 0$, which is why we see an increase in the level density for lower energies and spin in both Figure 2.4 and in Figure 2.3, which have been truncated at $E = 0.1\,\mathrm{MeV}$ in order to avoid this.

The level density was also investigated for a fixed spin for different isotopes of the $A = 20$ isobar, but no conclusive trends were found.
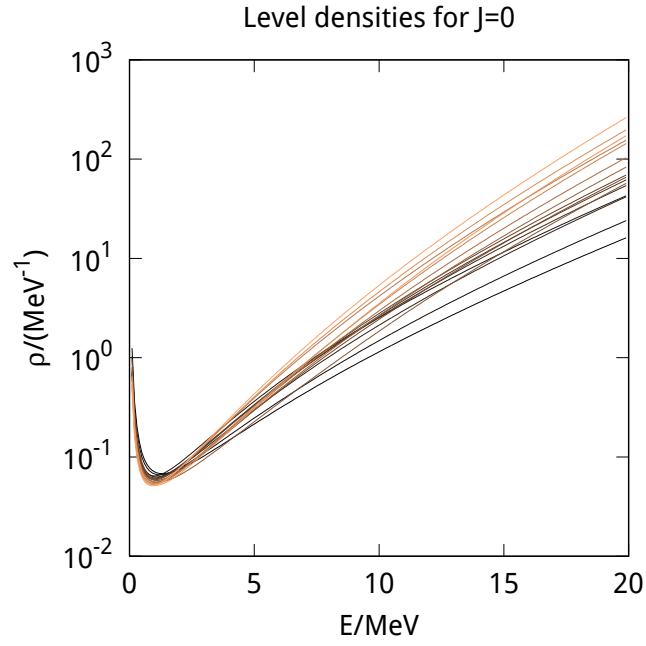
Figure 2.5.: *The level densities for* ^{17}Mg *to* ^{32}Mg*, where brigther lines correspond to heavier nuclei.*

On the other hand, for the isotope $Z = 10$, the level density for higher energies generally increases with additional neutrons, which is to be expected, since there are more ways to arrange the nucleons for a given excitation energy, this is illustrated in Figure 2.5, where the brighter lines correspond to heavier nuclei.

Transition Probabilities

The decay width $\Gamma_{\nu,l}$ into a given final energy interval $[E_f, E_f + dE]$ by particle ν with orbital angular orbital momentum l also depends on the transition probability $T_l(\epsilon_\nu)$.

One of the more well-known models of a transition probability by particle decay is the Gamow model for alpha decay, in which the mother nucleus (Z,N) is modeled as essentially being composed of a "ready-to-go" alpha particle and the daughter nucleus $(Z-2, N-2)$ and the probability to decay is given by the probability for the alpha particle to tunnel through the potential due to the daughter nucleus, with an additional factor depending on how often the alpha particle has a chance to tunnel.

This model is readily generalized to other particle decays: we may just as well imagine a proton being formed inside the mother nucleus (Z,N), and tunneling through the potential from the daughter nucleus $(Z-1, N)$.

In order to make this model quantitative, we need an actual potential. Approximating the charge distribution of the daughter and tunneling particle as spherical, we may model the potential due to electrostatic interaction as a simple Coulomb potential, which gives us

$$V = V_{\text{Col}} + \cdots = Z_1 Z_2 \frac{e^2}{r_{12}} + \dots, \tag{2.39}$$

in non-rationalized units. If we go ahead and assume that not only the charge distribution, but the potential as a whole is spherically symmetric, we can employ the standard procedure of separating the problem into a radial and angular part, where the radial potential is given by

$$V_{\text{r}} = Z_1 Z_2 \frac{e^2}{r_{12}} + \frac{l(l+1)\hbar^2}{2\mu r^2} + \dots \quad . \tag{2.40}$$

Here we still need additional terms to take the effective nucleon-nucleon intraction into account. The assumption of spherical symmetry also gives us the angular part of the wave function as a spherical harmonic, determing the angular distribution of the emitted particle in the center-of-mass frame.

The nuclear part of the potential used by CODEX is a proximity potential [4] [22]. Proximity potentials may be derived from a more general approximation method, in which two nearby surfaces are divided into several parallel surfaces, close enough to be approximated as semi-infinite, see Figure 2.6 [23]. The contributions from the different sets of parallel surfaces are assumed to be additive. The potential energy is calculated for these slabs, and factors to correct for the actual geometry are introduced. This approach is widely used in Casimir force calculations between objects of a more arbitrary shape [24]. This approximation is also known by "Derjaguin approximation" in other fields [23].

In the nuclear case, the situation is somewhat complicated by the fact that the form of the nucleon-nucleon interaction is unknown. As such, there exist several proximity potentials [25]. Dutt et. al. showed that 12 common proximity potentials were able to predict fusion barrier heights within 10% of the experimental values for asymmetric fusion reactions ranging from ^{12}C$+$ ^{17}O to ^{86}Kr$+$ ^{208}Pb [25]. Proximity-type potentials
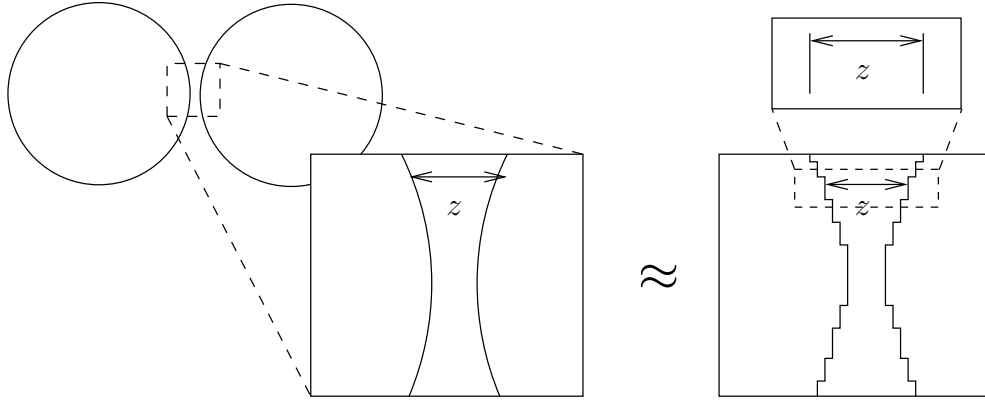
Figure 2.6.: *A schematic sketch of how the proximity approximation is carried out. Two close surfaces are approximated as a series of parallel surfaces, which in turn are approximated as infinite parallel surfaces, for which the potential energy is easier to calculate. This result is then summed up for all parallel surfaces.*

have also been used to study alpha and proton decay [26] [27], which is closer to our intended application[8].

The proximity potential is given by

$$V_{\mathrm{N}} = C\phi(\zeta), \tag{2.41}$$

where $\phi(\zeta)$ is the so-called *universal function*, which for a given nucleon-nucleon interaction is independent of the geometry of the nuclei in the proximity approximation. ζ is a unitless distance between the two nuclei, see below. Geometrical factors are contained in the proportionality "constant" C, which is given by

$$C = 4\pi\gamma b \frac{r_{c,1} r_{c,2}}{r_{c,1} + r_{c,2}} \tag{2.42}$$

where γ is the surface energy coefficient, which can be approximated by

$$\gamma = 0.9517(1.0 - 1.78260 \times I^2), \tag{2.43}$$

where $I = (N - Z)/A$ is the neutron excess.

We use the universal function by Blocki, 1997,

$$\phi(\zeta) = \begin{cases} -0.5(\zeta - 2.54)^2 - 0.0852(\zeta - 2.54)^3 & \zeta < 1.2511 \\ -3.437 \exp\left(-\zeta/0.75\right) & \zeta > 1.2511, \quad [22] \end{cases} \tag{2.44}$$

---

[8]It is not immediately obvious to the author if the assumptions of the proximity potential formalism applies to proton or alpha decay. It does however reproduce experimental half-lives to a reasonable degree, see e.g. Balasubramaniam and Arunachala [26], this is for emission from heavier nuclei, though.

where ζ is the distance between the two nuclear surfaces, normalized with respect to the typical surface diffuseness b of the nuclei, here taken to be $1\,\mathrm{fm}$ [22]. More explicitly, we have

$$\zeta = \frac{r - r_{\mathrm{sum}}}{b}, \tag{2.45}$$

where b is the surface diffuseness, and r_{sum} is roughly the sum of the radii of the two nuclei, so that $r - r_{\mathrm{sum}}$ gives the distance between the nuclear surfaces [22]. An effective sharp nuclear surface may be estimated by the formula

$$r_{\mathrm{sharp}} = 1.28A^{1/3} - 0.76 + 0.8A^{-1/3} \quad \mathrm{fm}. \qquad [22] \tag{2.46}$$

Equation 2.46 is used to estimate the radii of all nuclei, and as a result $r_{\mathrm{sharp}} = 1.32\,\mathrm{fm}$ for protons and neutrons, which is slightly different from the value of r_0 that is normaly used. In the proximity potential, it is preferable to use the *central radius* r_{c} rather than the effective sharp radius [22], which is given by

$$r_{\mathrm{c}} = r_{\mathrm{sharp}} \left(1 - \left(\frac{b}{r_{\mathrm{sharp}}} \right)^2 \right) \quad . \qquad [28] \tag{2.47}$$

Hence, $r_{\mathrm{sum}} = r_{\mathrm{c},1} + r_{\mathrm{c},2}$.

Since the proximity model takes the spatial extent of the nuclei into account, we modify the Coloumb-interaction accordingly, from that of a point particle to that of a homogenously charged, solid sphere

$$V_{\mathrm{C}} = \begin{cases} \frac{Z_1 Z_2 e^2}{r} & r > r_{\mathrm{ch}} \\ \frac{Z_1 Z_2 e^2}{r_{\mathrm{ch}}^2}(3 - (r/r_{\mathrm{ch}})^2) & r < r_{\mathrm{ch}}, \end{cases} \tag{2.48}$$

where we here use the more common formula for the charge radius, $r_{\mathrm{ch}} = r_0 A^{1/3}$.

In Figure 2.7, we illustrate the total potential of ^{20}Ne for tunneling of protons and neutrons. The individual contributions to the total potential may be discerned by looking at the potential for the emission of $l = 0$ neutrons (which are only affected by the proximity potential) and $l = 0$ protons (which have to tunnel through the sum of the Coulomb and the proximity potential). On this energy scale, the barrier the protons have to tunnel through is merely $2\,\mathrm{MeV}$ high, but since the proton separation energy for ^{20}Ne is $12\,\mathrm{MeV}$, it will only happen for excitation above $12\,\mathrm{MeV}$, as the proton does not have a positive energy otherwise. Neutrons with a positive energy and $l = 0$ do not have to tunnel at all, and exist as resonances above the potential barrier. The tunneling formalism does not apply in this case, and we instead use (2.54), which we discuss later.

We also see that the centrifugal part quickly dominates, essentially a result of protons and neutrons being relatively light particles: for α-decay, the centrifugal part is about a fourth of the values displayed above, and the l-dependence of the tunneling probability is not very significant for low l [29]. This strong l-dependence makes proton radioactivity a sensitive probe for the orbital angular momentum of valence protons for proton emitting nuclei [26]. However, in this case, it also poses a problem, since, for high l-values, it removes the potential well created by the Coulomb and proximity potential. Even for
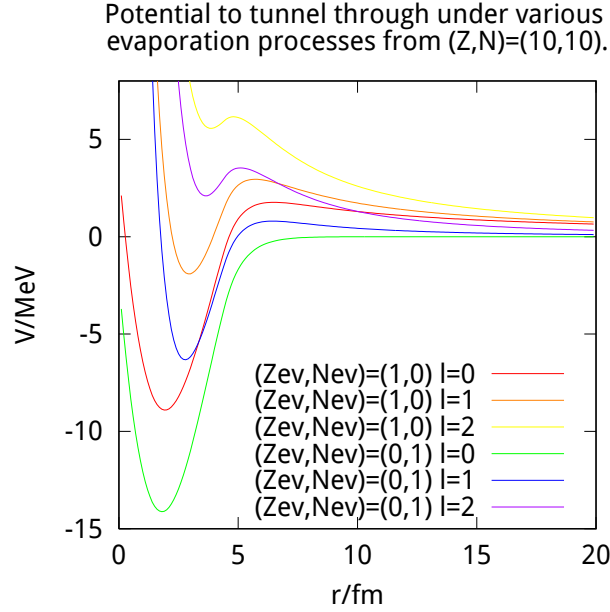
Figure 2.7.: *The potential used for tunneling of neutrons and protons with $l = 0,1,2$ from* ²⁰*Ne. The potential for $l = 0$ neutrons is exactly the proximity potential (2.44), while the $l = 0$ proton's potential show the sum of the proximity and Coulomb potential.*

moderate l values, it makes particles with low energy classically forbidden within the the radius of barrier (see Figure 2.7), which appears inconsistent with the picture of a preformed particle tunneling through said barrier. The solution adopted in this work is to assign probability zero to tunnel for particles that are classically forbidden within the nucleus. This will supress decay for higher l, since the bottom of the potential well rises as l does. For a higher l, the potential well disappears entirely[9].

Given the potential, the transition probability can be calculated in the WKB approximation as

$$T_l(\epsilon_\nu) = \exp(-2G), \qquad [13] \tag{2.49}$$

where

$$G = \sqrt{\frac{2\hbar}{\mu}} \int_{r_1}^{r_2} \sqrt{V_l(r) - \epsilon_\nu}\, dr. \tag{2.50}$$

---

[9]Another solution, attractive since we do not use the potential to estimate separation energies, is to model the strong interaction as an infinitely deep potential that cancels the centrifugal part, so that bound particles can always exist in the nucleus. The common $V = -\infty$ for $r < r_{\text{nucleus}}$ potential achieves this. Another solutions found in the literature is to have other, finite potentials below certain radii, but – in non-relativistic quantum mechanics – this goes against the assumption of spherical symmetry unless the effective nucleon-nucleon interaction depends on l so to exactly cancel the centrifugal part.

The classical turning points, r_1 and r_2, are the inner and outer radii for which the kinetic energy is equal to the potential energy. It should be noted that the WKB approximation is not, strictly speaking, valid for regions where the potential is approximately constant over several wave-lengths $\lambda = \frac{2\pi}{k}$, which will not be valid for at the turning points, since $\lambda \to \infty$. A somewhat more refined WKB approximation formula is

$$T_l(\epsilon_\nu) = \frac{1}{1 + \exp 2G}, \qquad [30] \tag{2.51}$$

which still suffers from the same short-comings as the previous formula. Nevertheless, the transition amplitudes calculated with the WKB formula are generally of the right order of magnitude, which should suffice for our purposes [31].

For $\epsilon > V_{\max}$, we can no longer view the emission as tunneling, because the particle passes "over" the barrier. Instead, we use

$$T_l = \frac{1}{1 + \exp\left(-\frac{2\pi}{\hbar\omega}(E - V_{\max}))\right)}, \tag{2.52}$$

where

$$\hbar\omega = \hbar \sqrt{\frac{1}{\mu}\left(\frac{d^2 V_l}{dr^2}\right)_{r_{\max}}}. \qquad [4] \tag{2.53}$$

We use yet another formula for $l = 0$ neutrons, which do not have a barrier to tunnel through, and for which Equation 2.52 cannot be applied, since no maximum exists. Instead, we use the transmission coefficient for transmission over a step

$$T_{0,\mathrm{n}} = \frac{4\sqrt{E}\sqrt{E + V_0}}{(\sqrt{E} + \sqrt{E + V_0})^2}, \tag{2.54}$$

where we use the depth $V_0 = 40\,\mathrm{MeV}$, the value being chosen to approximate the depth of the nuclear potential [32]. This was the formula used in CODEX.

The transmission coefficients corresponding to the potentials in Figure 2.7 are presented in Figure 2.8. We see that the $l = 0$ neutrons do not behave as expected, in that they have a lower transmission coefficient than both protons and $l = 1$ neutrons. We also see the very sudden increase of the transmission coeffiecients for higher l-values, a result of our choice to set the transmission probability to zero for $E < V_{l,\min}$ and to not cut the centrifugal potential below some r-value.

γ-decay The above discription concerns the tunneling of a nucleon or cluster through a potential barrier, and is thus not applicable to γ-decay.

Gamma transition rates are usually expressed in terms of a strength function, f_{Xl}, like

$$T_l(E) = E^{2l+1} f_{Xl}(E). \tag{2.55}$$

The factor E^{2l+1} factorizes out the energy dependence from semi-classical radiation theory, so that the strength function contains the nuclear information. X here refers to the type of radiation, electric or magnetic.
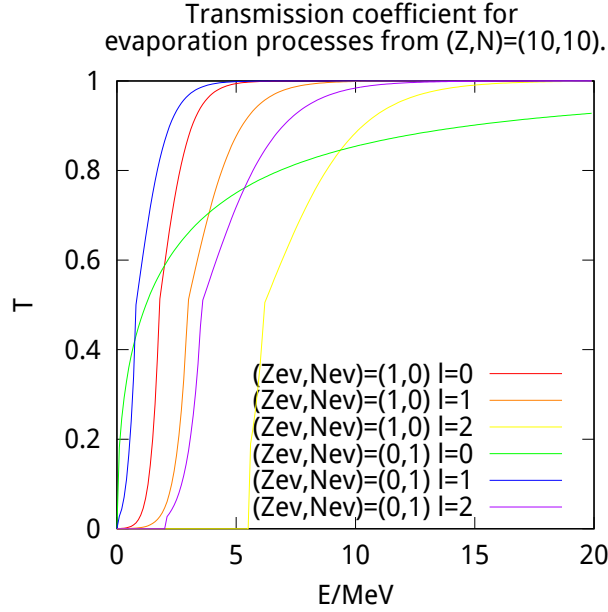
Figure 2.8.: *The transmission coefficients for evaporation of neutrons and protons with $l = 0, 1, 2$; from ^{20}Ne.*

There are many ways in which a nucleus can emit photons, and hence several kinds of strength functions. For our purposes, collective excitations are the most important, and the modes that dominate are the *Giant resonance*, in particular the $E1$, $E2$ and $M1$ modes [18]. These collective excitations are vibrational in nature, and give rise to Lorentzian strength functions.

The strength functions used in this work are

$$f_{E1} = \frac{ZN}{A} \frac{4e^2}{3\pi u\hbar} \frac{E_\gamma^4 \Gamma_{E1}}{(E_\gamma^2 - E_0^2)^2 + (E_\gamma \Gamma_{E1})^2}$$
$$f_{E2} = \frac{6Ze^2}{25\pi\hbar^3 u} R^2 \left(1 + \frac{5}{2}\frac{b^2}{R^2}\right) \sum_j \frac{1}{2} \frac{E_\gamma^4 \Gamma_{E2}}{(E_\gamma^2 - E_{0j}^2)^2 + (E_\gamma \Gamma_{E1})^2}, \tag{2.56}$$

where $R = r_0 A^{1/3}$ is the nuclear radius and b the surface diffuseness, a parameter also used in the proximity potential. The presence of Z and N in the above equations are to account for the number of nucleons participating in the excitation [33]. The peak values are given by

$$E_{0,E1} = \frac{80}{A^{1/3}} \text{MeV},$$
$$E_{01,E2} = \frac{63}{A^{1/3}} \text{MeV} \frac{130}{A^{1/3}} \text{MeV}. \tag{2.57}$$

The value $80/A^{1/3}$ is supposedly a good fit for medium to heavy weight nuclei [33], while

the $63/A^{1/3}$ and $130/A^{1/3}$ are too diffuse to reliably observe in light nuclei [34] [35]. As such, it may be desirable to use other values for light nuclei, as well as adding in the possibility of an $M1$-transition.

2.2. Finite-Range Droplet Model

The Finite-range droplet model with parameters fitted to nuclear data in 1995 [21] was used to determine the macroscopic contributions to mass excesses. The macroscopic part of the FRDM is in essence– like all macroscopic mass formulas– a refined version of the *semi-empirical mass formula* (SEMF). Just like the SEMF, the FRDM contains volume, surface, Coloumb, asymmetry (in the form of a Wigner term) and pairing terms. It also contains numerous other terms, not discussed here, but see the original literature [21].

Important to note is that our macroscopic energy was obtained for spherical nuclei, while the model parameters of the FRDM were fitted to experimental mass exesses while using deformations from a previous iteration. As such, our calculated macroscopic mass excesses do not contain deformation energies, and when we calculate the microscopic (pairing and shell energy), we actually calculate

$$E_{\text{exp}} - E_{\text{mac}}(\text{sphere}) = E_{\text{s+p}} + E_{\text{deformation}}, \qquad (2.58)$$

which means that for deformed nuclei, our estimate of shell and pairing effects will include contributions from the deformation energy. Since the rest of the code does not take deformations into account, this is not really an additional contraint.

3. The Code

The CODEZ code, based on CODEX [4], contains models for the various quantities needed in statistical models. It is written to be extendable and to a large extent modular, so that the various models can easily be replaced. Details on the specific models may be found in section 2.1. To achieve this modularity, the code is written in C++ and makes use of *object-oriented* programming concepts.

The program is roughly structered as follows: Decay processes are specified by model objects, which contain models for calculating transition probabilities to possible final states. "Probabilities" here refers to $d^2P_\nu/dtdE$, the probability to decay to a final state in energy interval dE during the time dt by the process ν. The probabilities do not need to be normalized. The model objects implement a function that for a given energy discritization tabulates a specification of the decay (The excitation energy of the final state, the spin of the final state, the particle ν which has been emitted in the decay, its orbital angular momentum) along with a corresponding cummulative probability. A complete table of cummulative transition probabilities and final states is generated by looping over all model objects.

A de-excitation step may then be performed by drawing a random number between 0 and the final cummulative probability, and looking up the corresponding decay in the table. Several one-step decays from the same state may thus be performed with little extra computational costs.

The tabulation of decay probabilities, the deexcitation and the models all compile to different object-files, which are linked to produce exectable files with various purposes – such as deexciting a nucleus until its excitation energy reaches a certain value, finding the most common decay channel for several different nuclei with given excitation energies, export level densities, etc. This removes the need to excessively control the program flow in the individual main-files, which makes the code easier to read, since it mostly describes the physics – although it may lead to some code duplication.

The next section describes the individual executable programs, and demonstrates how they may be used together to solve more complicated tasks.

3.1. Programs

The CODEZ code contains three types of subprograms: programs to generate lists of nuclei, programs that run on a list of nuclei, and programs that process the output of

the latter programs. The different kinds of programs may be used in a pipe, like

list | run | process

3.1.1. List generating programs

The first kind of program simply generates lists of nuclei to perform calculations for. The output of these programs are of the form illustrated by this example output:

#comment
∗Event 1
Z11 N11 E11 J11 px11 py11 pz11
Z12 N12 E12 J12 px12 py12 pz12
∗Event 2
Z21 N21 E21 J21 px21 py21 pz21

where Z,N,E,J,p specify the proton number, neutron number, excitation energy, spin and 3-momentum of the nucleus. If no event numbers are present, each line is assumed to be a separate event. Simpler lists could easily be written by hand, but the list-type programs make it possible to run a specific calculation (as specified by a "run-type" program) easily for a range of nuclei, or nuclei generated by a specific process.

NUCLIST

The NUCLIST program simply generates a list of nuclei for a given N, Z or A range; with a given excitation energy, spin and initial momentum. This program can be used to determine spectra from excited nuclei of certain isotopes, isobars and isotones.

Each nucleus is placed in a separate event.

QUASI

This program simulates a quasi-elastic scattering event, producing an excited prefragment as well as the participating knocked-out cluster and target fragment. The beam energy, the number of events, the colliding nuclei must be specified, and the excitation energy and spin of the spectator prefragment may be specified.

The target and cluster fragments are assumed to be in their ground states, which should be a good assumption for lighter clusters and targets.

Each scattering event is placed in a separate event.

3.1.2. Programs to run on nuclei-lists

These programs can be run on a list produced by the above programs in order to perform various calculations.

SPECTRA

This program, primarily intended to be run on the output of NUCLIST, prints the probabilities of various decay modes from the initial states specified by the nuclie-list. The `-details` flag controls to which level of detail the spectra are printed. This is essentially a program to illustate the decay widths as calculated by the program, and hence it ignores event numbers.

DEEXCITE

The bulk work of an event generator is performed in this program. Each nucleus in each event in the input file is deexcited until it is below a specified threshold energy, or, alternatively, a given number of deexcitation steps can be specified. The resulting nuclei are printed to a new list, with the event number inherited from their mother nuclei. Combined with the output of QUASI and the post-processing program LIST2GUN, this program is able to act as an event generator for GEANT4 through the wrapper GGLAND.

RHO

This program produces a *tab-separated value* (tsv) file of the level density for each nucleus in the input list. By default, only the Z, N and J of the nuclei is used, and the level density is plotted for a range of excitation energies, rather than the actual energy of the nuclei in the input files, which are ignored in this mode.

POT

Like RHO, this program produces a *tab-separated value* (tsv) file for each nucleus in the input list, this time of the potential a particle has to tunnel through to be emitted by the nuclei in the list. The potential for a given particle-decay can be exported for a range of l values.

4. Results

4.1. Prefered Decay Channels

As a first qualitative test to the code, we consider the decay of a wide range of nuclei, from $(Z,N) = (10,10)$ to $(90,130)$. A list of all eligible nuclei was generated by NUCLIST, for 4 different exciation energies, $E* = 5, 10, 15, 20\,\text{MeV}$, and $J = 0$. The most likely decay channel of these nuclei were then calculated with SPECTRA.

The results, which were run though an OCTAVE script to plot each nuclei on a chart, is presented in Figure 4.1 and Figure 4.2. In the first picture, we see how the nuclei close to the line of β-stability preferentially decay by emitting a gamma at $E^* = 5\,\text{MeV}$, but already at $E^* = 10\,\text{MeV}$, most nuclei are *particle unstable*. Proton separation energies for stable nuclei are in the range of $7 - 9\,\text{MeV}$ [36]. We also see a distinct odd-even effects: nuclei with an even number of a nucleon tend to have higher separation energies, due to pairing. Finally, we note that neutron evaporation is by far more common across the chart, which is to be expected, since protons have to tunnel through the Coulomb barrier. Note however that our Fermi-gas level density will not be valid for low energies, where the discreteness of the levels should be taken into account – these results should be viewed more like a benchmark of the code, than physical predictions.

At yet higher energies, a few potential oddities appear. According to CODEZ, relatively neutron rich nuclei decay by emitting a proton – neutron rich meaning below the region of "proton instability", and in one case even below the line of β-stability! It could perhaps be that once the energy is high enough for protons to readily tunnel through the Coulomb barrier, a high level density in the daughter nucleus makes the program favor proton decay. This kind of reasoning could also be applied to alpha particles, which have a higher Coulomb barrier, but may be allowed to dominate at sufficiently high energies if the level density of the daughter is favorable. However, we see a few nuclei, $(Z,N) = (17,15); (32,33); (33,34)$ that decay by proton evaporation at $E^* = 10\,\text{MeV}$, then by α at $E^* = 15\,\text{MeV}$ and by proton at $E^* = 20\,\text{MeV}$, which could indicate that there is no simple energy threshold above which more *density favored* decay start to dominate. However, α and protons have vastly different centrifugal barriers, which perhaps may explain the more complicated shifts in prefered decay modes.

These results where compared with the output of another nuclear reaction code, TALYS [5]. Specifically, TALYS-1.73 was used, since it adds a keyword to make TALYS print the
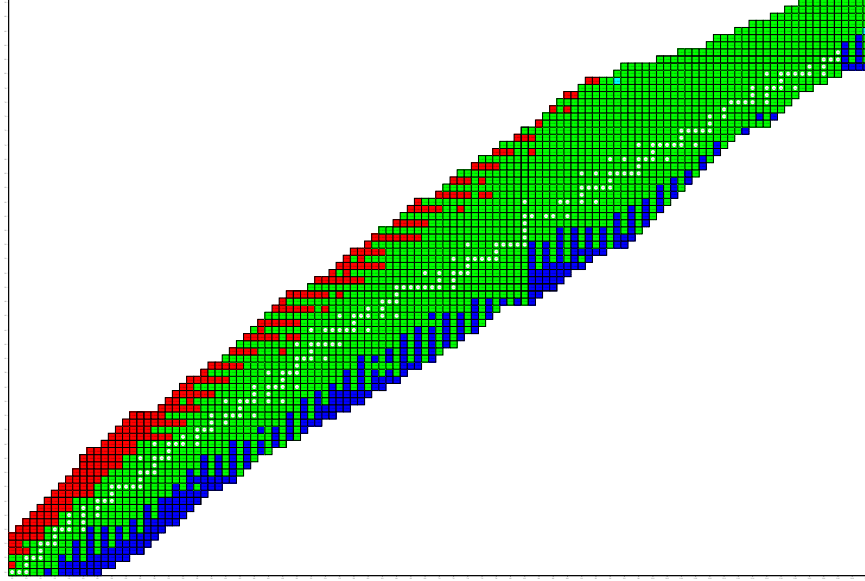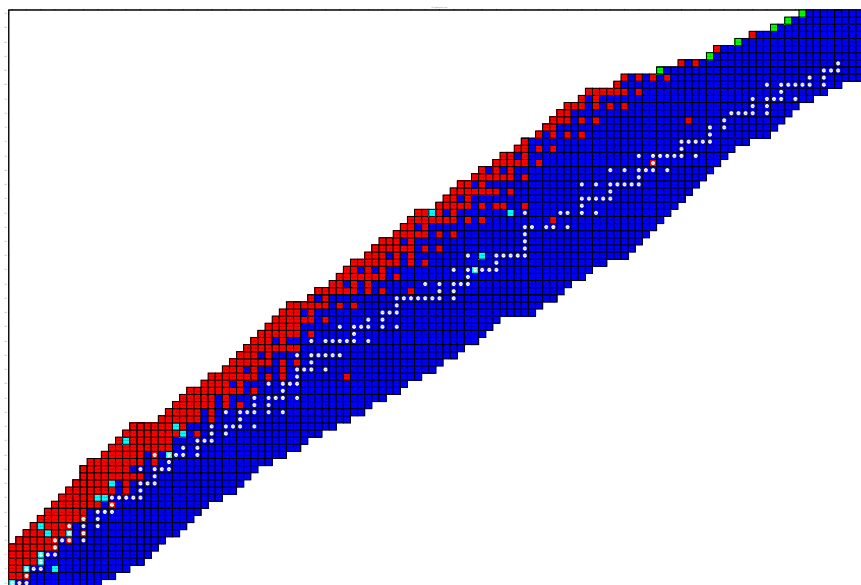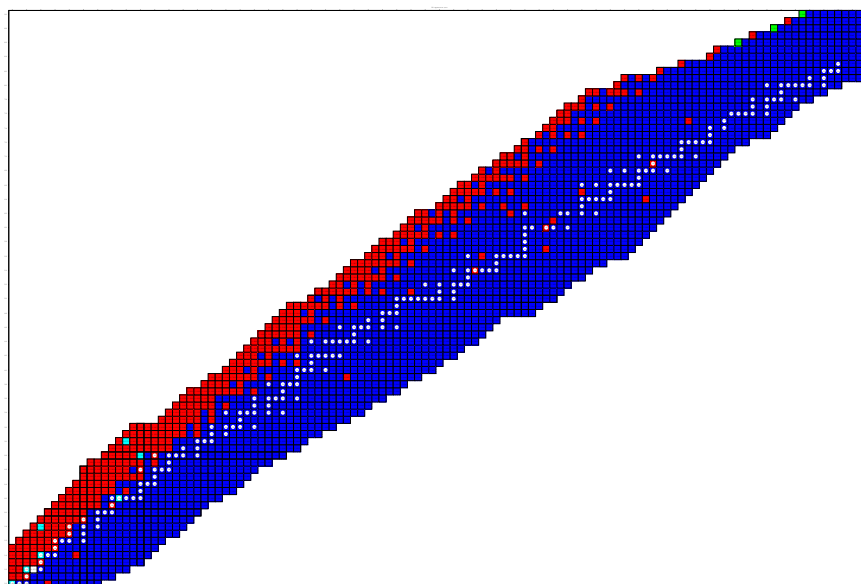
(a) $E^* = 5\,\mathrm{MeV}$
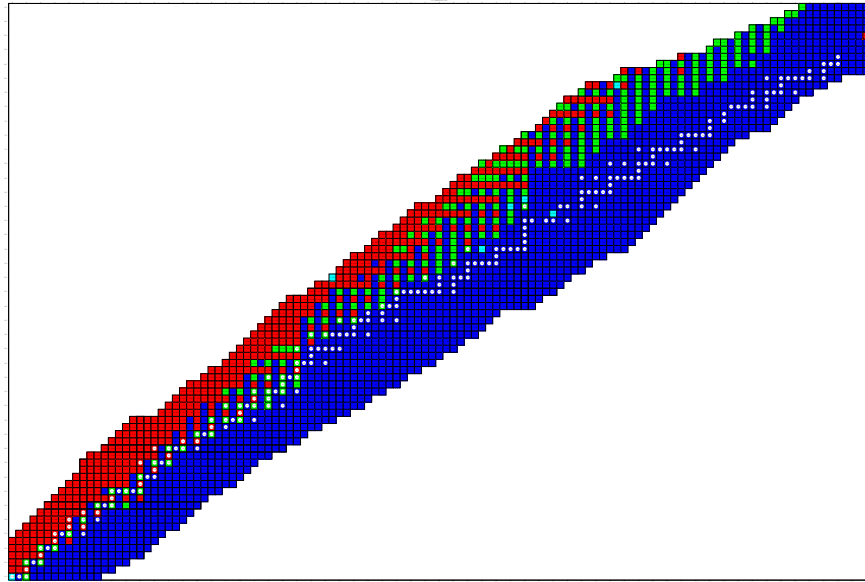
(b) $E^* = 10\,\mathrm{MeV}$

Figure 4.1.: *The prefered decay mode of a wide range of nuclei according to CODEZ, for various excitation energies and $J = 0$. The dominant decay mode is indicated as follows: blue=neutron, red=proton, green=gamma, cyan=alpha. Nuclei that are beta-stable in their ground-state are marked with a white dot.*

(a) $E^* = 15\,\mathrm{MeV}$

(b) $E^* = 20\,\mathrm{MeV}$

Figure 4.2.: *The prefered decay mode of a wide range of nuclei according to CODEZ, for various excitation energies and $J = 0$. The dominant decay mode is in-dicated as follows: blue=neutron, red=proton, green=gamma, cyan=alpha. Nuclei that are beta-stable in their ground-state are marked with a white dot.*

Figure 4.3.: *The prefered decay mode of various nuclei according to TALYS, for the excitation energy $E^* = 20\,\mathrm{MeV}$. The dominant decay mode is indicated as follows: blue=neutron, red=proton, green=gamma, cyan=alpha. Nuclei that are beta-stable in t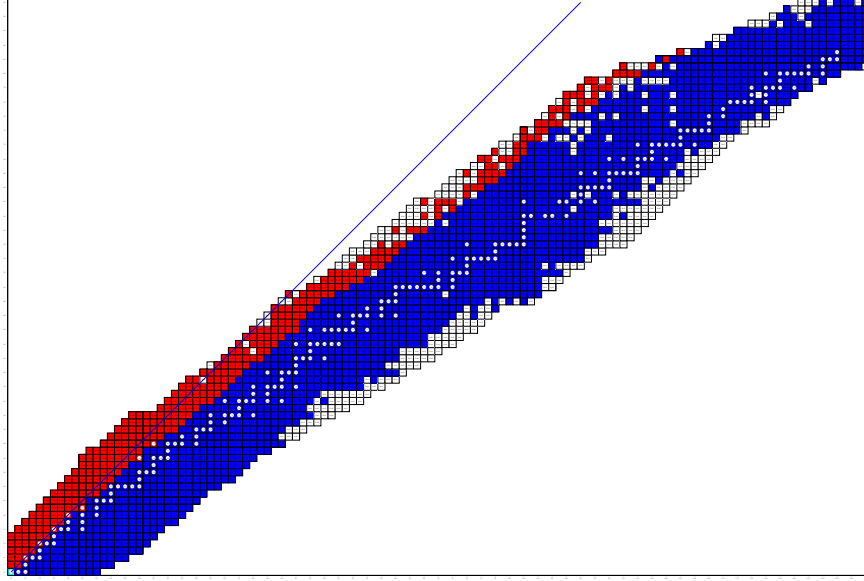heir ground-state are marked with a white dot. Nuclei which had no suitable level near $E^* = 20\,\mathrm{MeV}$ are displayed in white.*

emission spectra from a specific excited level[1]. The results of the TALYS simulations can be seen in Figure 4.3, for $E^* = 20\,\mathrm{MeV}$. Since TALYS uses discrete levels when these are known (complemented with theoretical models up to the 100th level [5]), it is not always able to populare a $E^* \approx 20\,\mathrm{MeV}$ level, and for these nuclei (white in Figure 4.3), no spectra was simulated. No restriction on the spin of the levels were imposed, and in the cases where two levels were suitably close to $E^* \approx 20\,\mathrm{MeV}$, the highest level was chosen. This is also why we only compare with TALYS for higher excitation energies.

We see that the spectra are in qualitative agreement, and that the oddities of the CODEZ output is not present in the TALYS results, which one the whole has a less jagged boundary between the region of proton and neutron instability.

---

[1]Thanks to Arjan Koning for implementing this!

Nucleus	S_p	S_n	S_α (MeV)
^{28}F	19.0	-0.228	16.7
^{28}Ne	21.0	3.90	10.3
^{28}Na	15.3	3.54	11.0
^{28}Mg	16.8	8.50	11.5
^{28}Al	9.55	7.72	10.9
^{28}Si	11.6	17.2	9.98
^{28}P	2.06	14.5	9.53
^{28}S	2.50	21.5	9.10

Table 4.1.: *The separation energies of nuclei on the $A = 28$ isobar, for proton, neutron and alpha-particle emission.*

4.1.1. A more detailed spectra of the $A = 28$ isobar.

In order to investigate how the region of proton and neutron instability evolves with higher excitation energies, we look at the particle spectra of the $A = 28$ isobar. This isobar was chosen since it displays some of the anomalous behavior discussed above, and since we eventually want to focus on lighter nuclei when we later apply the code. The behaviour for lower energies is illustrated in Figure 4.4. ^{28}F is neutron unbound, while the other nuclei start to decay dominantly by neutron and proton emission almost as soon as they pass over the separation energies, which is presented in Table 4.1. At even higher energies, as presented in Figure 4.5, alpha evaporation starts to become energetically possible, and also – apparently – tritium evaporation, although that has a low probability of occuring. At yet higher energies, Figure 4.6, the probabilty for alpha decay starts to decrease again – possibly due to evaporation of partilces in higher l-states becoming possible for the lighter particles. For comparison, the output spectra from TALYS at $E^* = 20\,\text{MeV}$ is presented in Figure 4.7. Notably, the α-branching ratio is significantly lower for ^{28}Si.

To investigate how the individual decay modes vary with energy, we finally take a look at the full, energy dependent emission spectrum of a single nucleus. To see how the α-decay mode manages to compete with proton and neutron evaporation, we have plotted the likelihood of ^{28}Mg emitting protons, alphas and neutrons, for various l; see Figure 4.8 and Figure 4.9. As we see in these figures, which shows the energy cost off emitting the particles[2], $E_i^* - E_f^*$, each particle has a most likely excitation energy to be emitted at. This is due to the fact that highly excited particles "saturate" their transmission coefficients, one l at a time, but because the lowest energy to tunnel through the centrifugal barrier (in our model) goes like $l(l + 1)$, the particles are only able to

---

[2]We plot $E_i^* - E_f^*$ rather than the kinetic energy of the emitted particle, $E_i^* - E_f^* - S$, in order to shift the graphs so that the probabilities become non-zero at $\Delta E = S$, which makes it easier relate the likelihoods of emission to the excitation energy of the mother nucleus. Note however that the relative emission probabilities are unrelated to the excitation energy of the initial state provided that it has enough energy to emit the most likely particle: the $\rho(E_i^*, J_i)$ cancel each other.
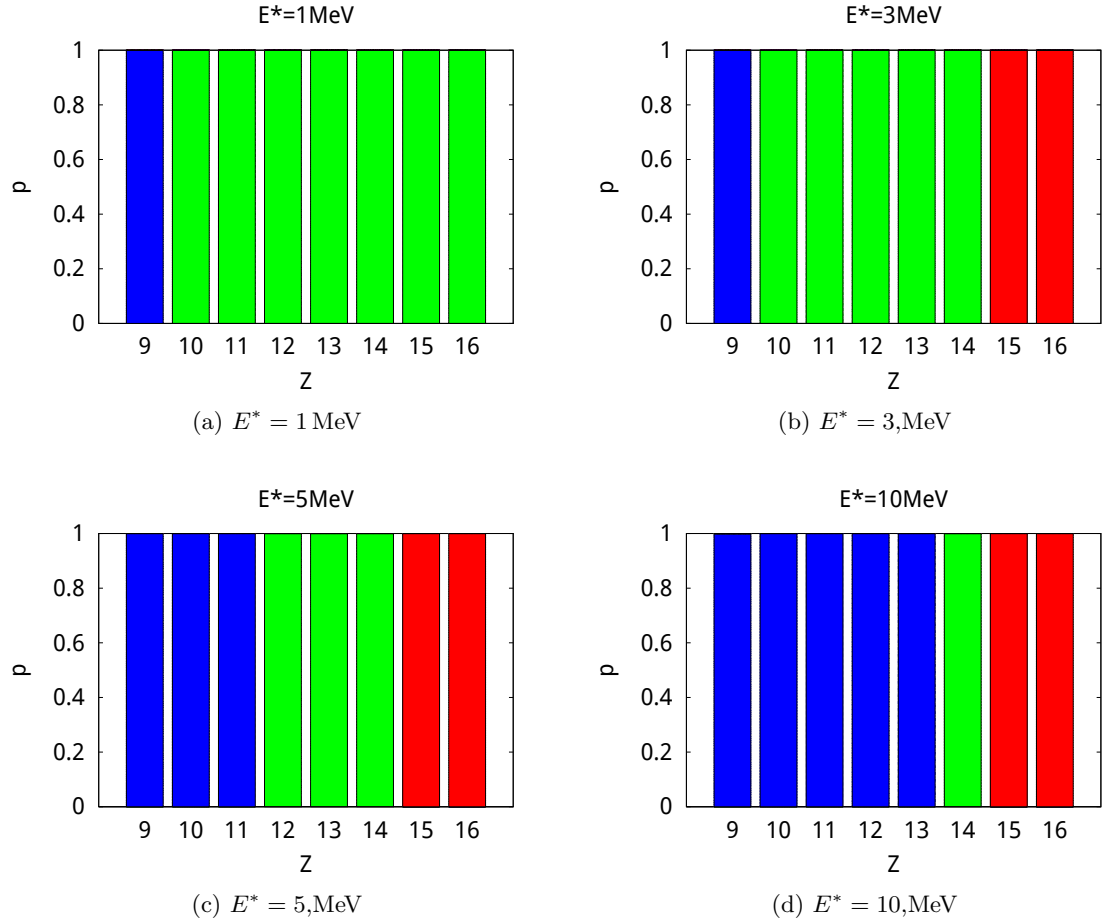
(a) $E^* = 1\,\mathrm{MeV}$

(b) $E^* = 3{,}\mathrm{MeV}$

(c) $E^* = 5{,}\mathrm{MeV}$

(d) $E^* = 10{,}\mathrm{MeV}$

Figure 4.4.: *The branching ratios for various decay modes at various energies for nuclei in the $A = 28$, according to* CODEZ. *The spin is $J = 0$ in all cases. The energies have been chosen to display changes in the spectrum. The colors signify the different decay modes: blue=neutron, red=proton, green=gamma.*
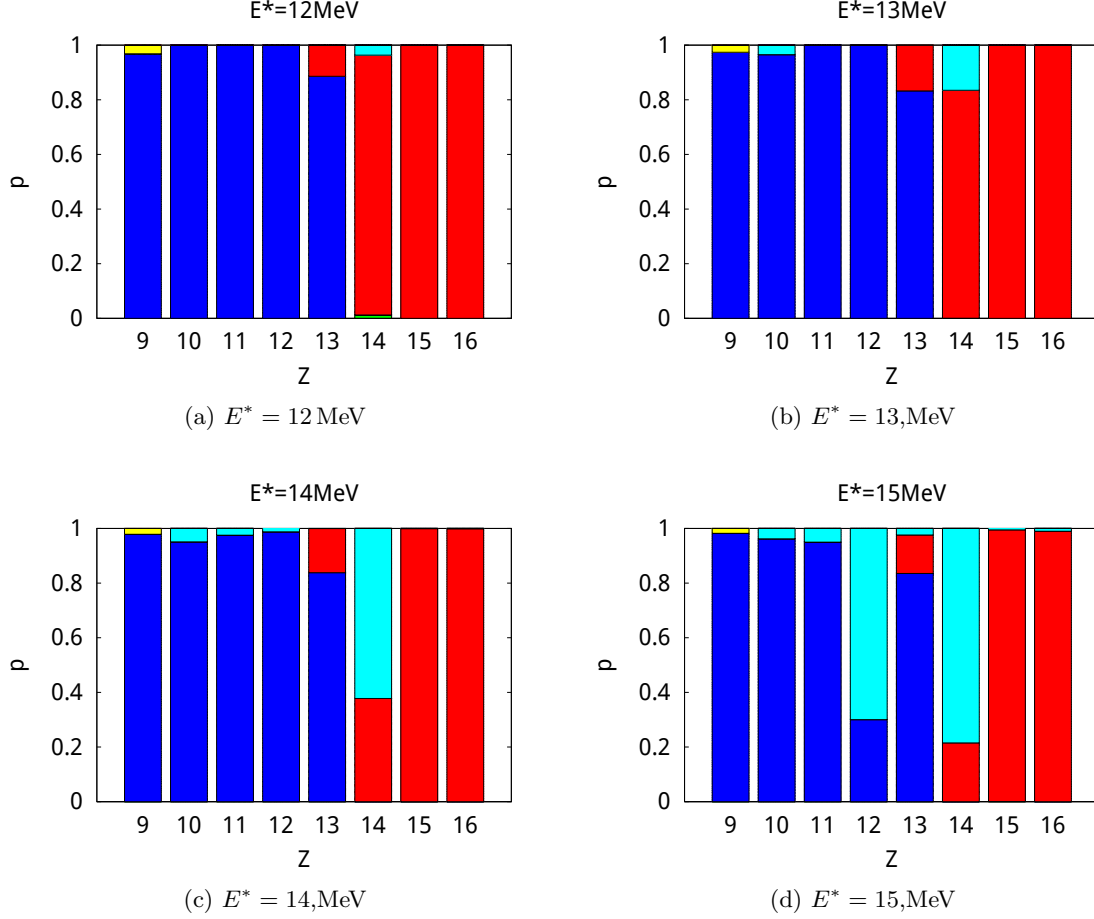
(a) $E^* = 12\,\text{MeV}$

(b) $E^* = 13,\text{MeV}$

(c) $E^* = 14,\text{MeV}$

(d) $E^* = 15,\text{MeV}$

Figure 4.5.: *The branching ratios for various decay modes at various energies for nuclei in the $A = 28$, according to CODEZ. The spin is $J = 0$ in all cases. The energies have been chosen to display changes in the spectrum. The colors signify the different decay modes: blue=neutron, red=proton, green=gamma, yellow=triton, black=deuteron*
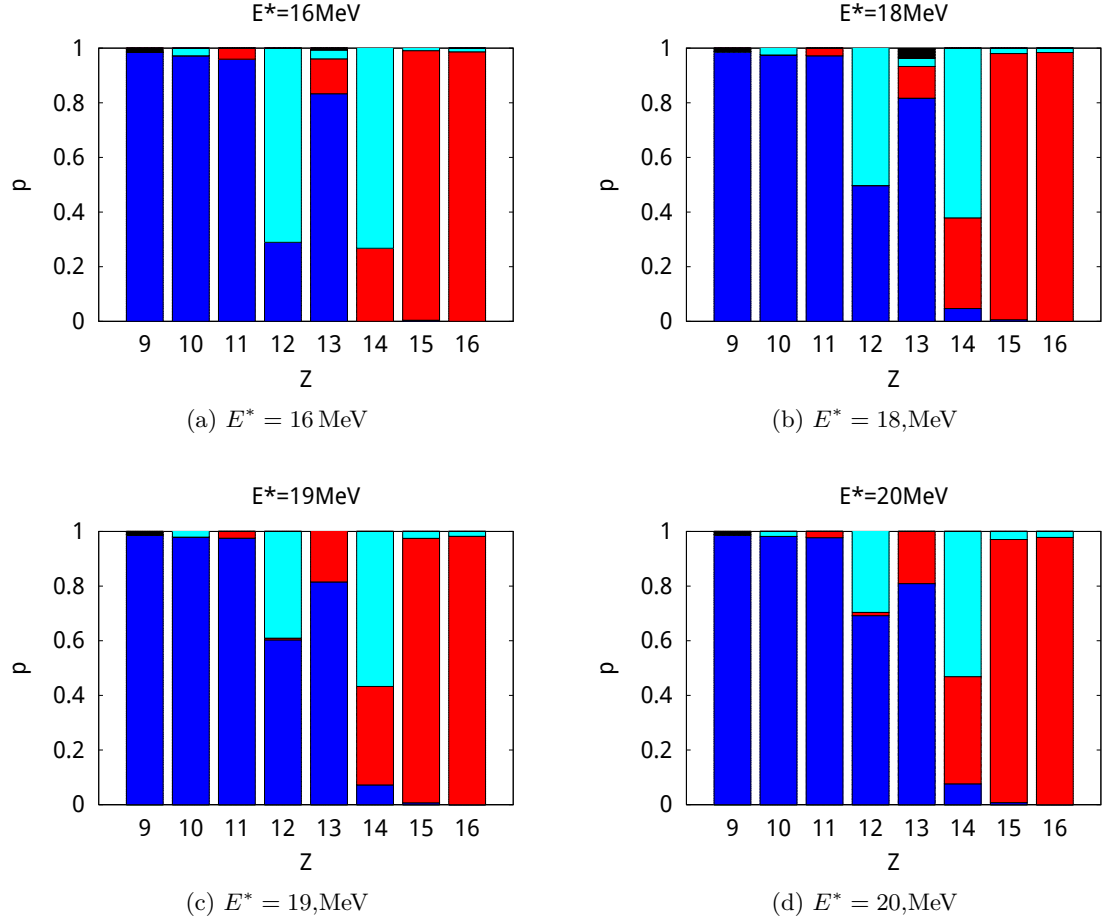
(a) $E^* = 16$ MeV

(b) $E^* = 18$,MeV

(c) $E^* = 19$,MeV

(d) $E^* = 20$,MeV

Figure 4.6.: *The branching ratios for various decay modes at various energies for nuclei in the $A = 28$, according to CODEZ. The spin is $J = 0$ in all cases. The energies have been chosen to display changes in the spectrum. The colors signify the different decay modes: blue=neutron, red=proton, green=gamma, yellow=triton, black=deuteron*
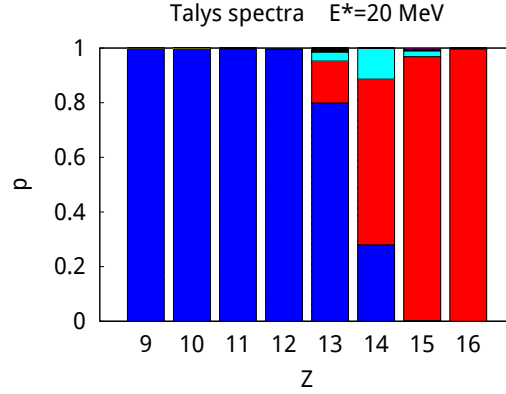
Figure 4.7.: *The branching ratios for various decay modes at $E^* = 20\,\text{MeV}$ for nuclei in the $A = 28$ isobar, according to TALYS. The colors signify the different decay modes: blue=neutron, red=proton, green=gamma, black=deuteron. The spin has been determined by TALYS, which populates discrete levels close to $20\,\text{MeV}$. Plotted is the decay modes from the highest such level.*

saturate a relatively low number of T_l's until they carry away so much energy that $\rho(E_f^*)$ becomes negligable in comparison to its value at higher E_f^*. Alpha particles, which have a lower centrifugal barrier, are able to saturate five l-values, while protons and neutrons only saturate two, which is reasonably given that $4(4+1)/(2(2+1)) = \frac{10}{3} \approx 4$, which is the ratio relating the nucleon and alpha centrifugal barrier. We also see that each l for neutron and proton emission has two curves, related to the fact that there are two ways to couple the spin of the nucleons (the initial state has $J = 0$). The alpha particle, being a spin zero particle, only has one curve for each l.

In short: a particle carrying away a lot of energy will easily tunnel, but the level density of the final state is much, much higher if the particle carries away just a small amount of energy, and thus high energy emission is effectively supressed, and we get a peak in the emission probabilities for the respective particles. Once our excitation energy is above these peaks, they may be emitted by the most likely way, and hence that probability gets saturated. That being said, the branching ratios can of course benefit from less likely ways to emit, and excitation energies beyond the peak makes the tail of the distribution available for the decays, but we do not expect to see dramatic swings like in the alpha spectrum for ^{28}Mg between $14\,\text{MeV}$ and $15\,\text{MeV}$ in Figure 4.5, which coincides rather nicely with the peak in Figure 4.9.

4.2. Gamma Multiplicities

As an interesting application of the code, we have investigated how γ-rays are produced in a quasi-elastic $(p,2p)$-event between ^{17}N and a proton target propagate through parts

Figure 4.8.: *The simulated probability that* ^{28}Mg *decays by proton emission (4.9a) and neutron emission (4.9b), respectively.*
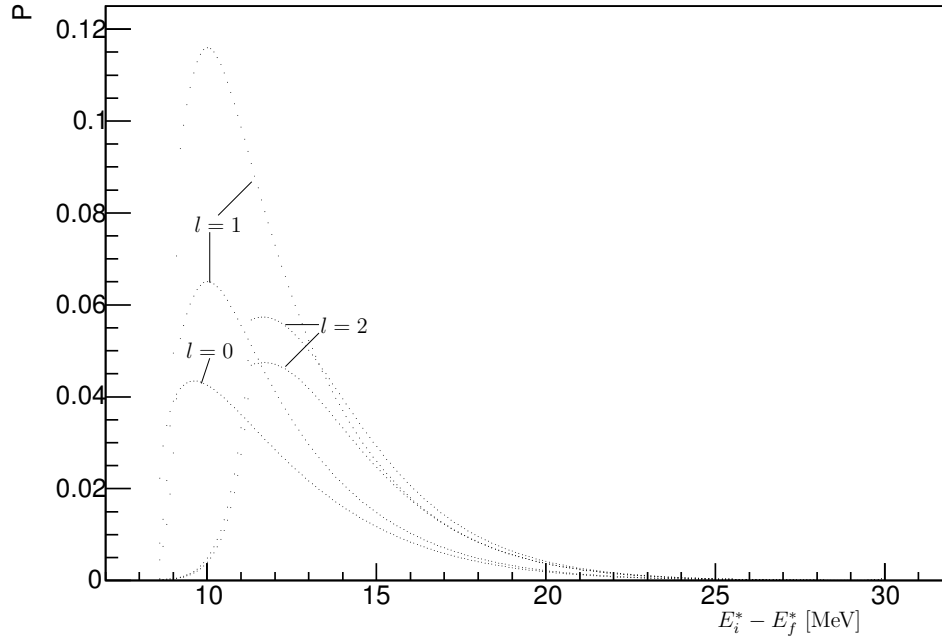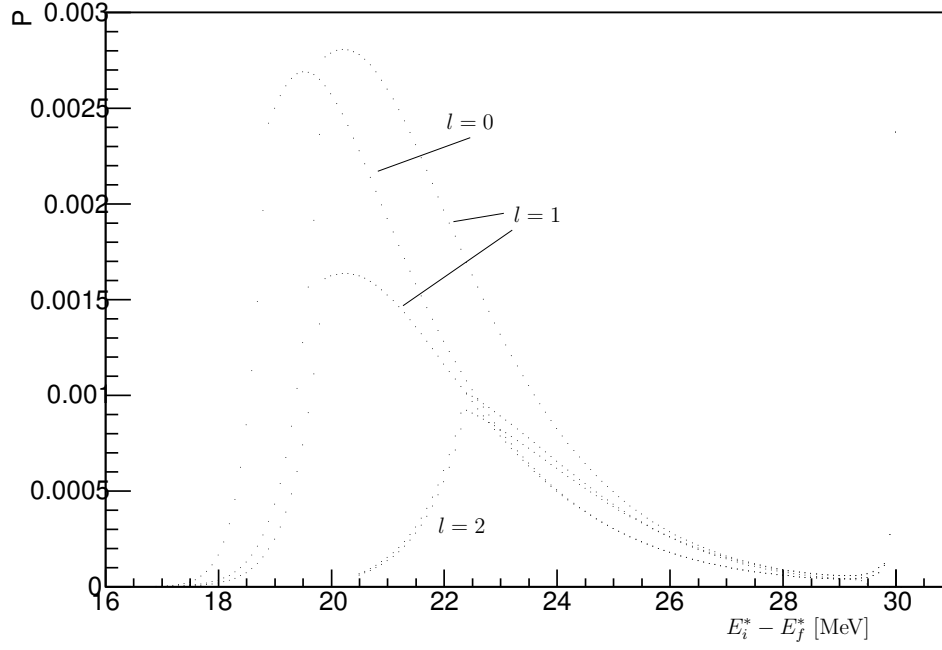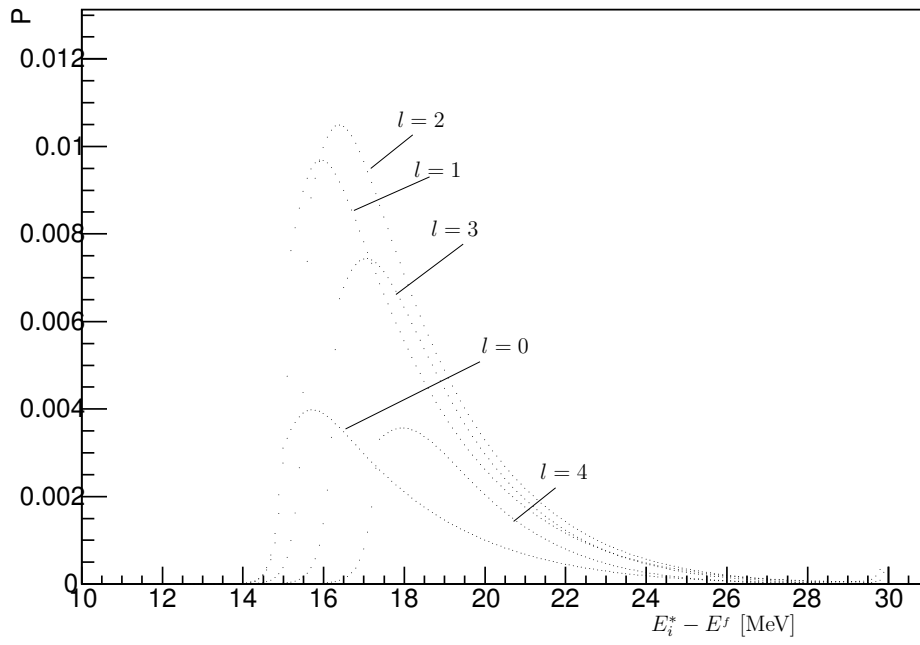
Figure 4.9.:   *The simulated probability that* ^{28}Mg *decays by alpha emission.*

of the *S393* experimental setup in Cave C at GSI. The ^{17}N nucleus had a kinetic energy of $419 \, \text{MeVA} = 7123 \, \text{MeV}$.

In order to compare CODEZ with the experimental data, its output was propagated through the experimental setup described in Table 4.2 by the Monte-Carlo GEANT4 – used through GGLAND. Furthermore, in order to account for the fact that photons Compton-scatter in the Crystal ball detector, energy deposits in nearby crystals are summed up according to an *addback routine*.

An addback routine is a heuristic method intended to compensate for the fact that γ-rays do not necessarily deposit all of their energy in one crystal. There are several ways to address this[3], but since we are interested in comparing our simulations with experimental data, we will use this algorithm:

- Remove energy depositions over $10 \, \text{MeV}$ (they are too large to likely be photons)

- Take the highest of the remaining energy depositions.

- Add to this energy the energy deposited in neighbouring crystals at most $30 \, \text{ns}$ before or after the primary deposit, and remove these deposits afterwards. The resulting energy is taken as the total energy the γ-ray deposited in the Crystal Ball.

- Repeat until all energy deposits are exhausted.

In addition, it was required that the energy deposited be greater than $0.1 \, \text{MeV}$: the real detector will have some threshold energy, and a lot of low energy electrons are produced in the simulations, so it is both practical and realistic to impose such a limit. The value used is somewhat arbitrary, but is low in relation to typical values.

This algorith was applied to the output of several GEANT4 simulations for different initial excitation energies. The resulting E_γ energies, togehther with the actual gamma energies, are plotted in Figure 4.10. We note that the identified gamma spectrum does not change notably with the excitation energy in this range, while the actual gamma spectrum contains a larger number of outliers for higher excitation energies.

That being said, what is emitted by the excited nucleus and what reaches the detectors are two different things. Neither of the figures in Figure 4.10 necessarilly tell us how much energy γ-rays actually deposited in the Crystal Ball.

Finally, as a test of the addback routines ability to reconstruct the number of γ-rays emitted in an event, we have in Figure 4.11 the number of times γ-rays were identified, and the number of times they were actually generated in the reaction. Again, we see that what is identified has little to do with what is emitted in the actual simulated reaction.

That being said, it is not obvious that the number of photons CODEZ emits is entirely realistic, since the discreteness of the level density should be apparent at the energies where γ-rays are preferentially emitted. There were also a high number of low energy deposits attributed to electrons in the simulation. These so-called δ *electrons* are secondary radiation produced as a result of charged particles ionizing the medium they

---

[3]see for example Simon 2013 [37] for an evaluation of a few different methods

Table 4.2.: *The simulated experimental setup, with detectors, the positions of their center, and the string used to place them in GGLAND. The axes are oriented so as to produce a right-handed coordinate-system with z in the beam direction, and y pointing upwards. Rotations refer to rotations around these axes with respect to the origin. The Crystal Ball covers the area around the reaction, which is located at the origin in between the thin silicone strip detectors (SST 3–6).*

Detector name	Position	GGLAND-string
SST-1	$z = 11\,\mathrm{cm}$	`-sst-1=z0=11cm`
SST-2	$z = 14\,\mathrm{cm}$	`-sst-2=z0=14cm`
SST-3	$y = 2.05\,\mathrm{cm}$	`-sst-3=z0=2.05cm,roty=90deg`
SST-4	$y = -2.05\,\mathrm{cm}$	`-sst-4=z0=-2.05cm,roty=90deg`
SST-5	$x = 2.05\,\mathrm{cm}$	`-sst-5=z0=2.05cm,roty=90deg,rotz=90deg`
SST-6	$x = -2.05\,\mathrm{cm}$	`-sst-6=z0=-2.05cm,roty=90deg,rotz=90deg`
Crystal Ball	At the origin	`-xb=z0=0cm`
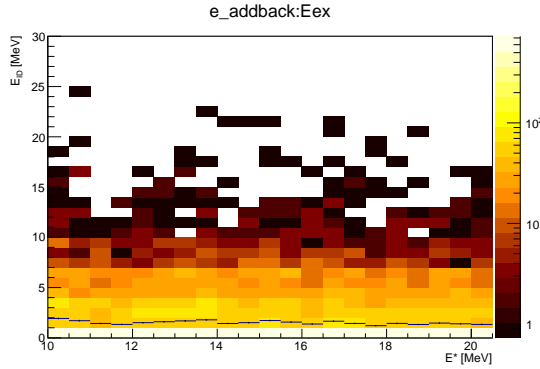
(a) The identified γ energy.
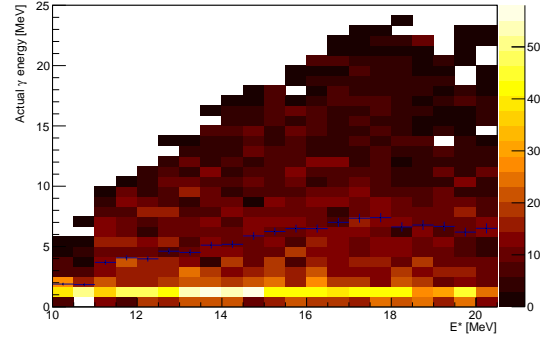
(b) The actual energy the γ-rays were produced with.

Figure 4.10.: *The gamma-multiplicities from simulations with ^{17}N at a kinetic energy $T = 7123\,\mathrm{MeV}$ undergoing a quasi-elastic (p,2p) reaction with a proton at rest in the origin. The simulations were performed for prefragment excitation energies $E*$ in the interval $[10,20]\,\mathrm{MeV}$ with a $0.5\,\mathrm{MeV}$ spacing. The y-axis shows the gamma energy deposits – event by event – as determined by the addback routine and the actual gamma energy, respectively.*
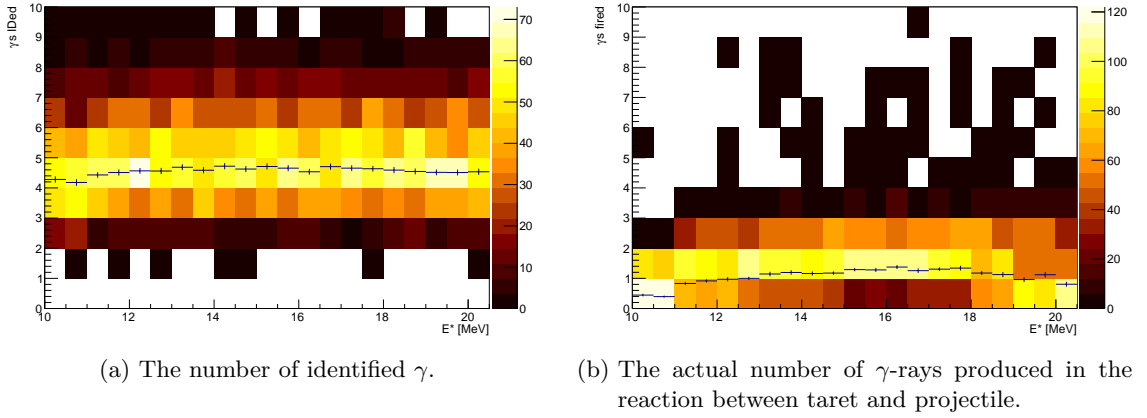
(a) The number of identified γ.

(b) The actual number of γ-rays produced in the reaction between taret and projectile.

Figure 4.11.: *The gamma-multiplicities from simulations with* ^{17}N *at a kinetic energy* $T = 7123$ MeV *undergoing a quasi-elastic* (p,2p) *reaction with a proton at rest in the origin. The simulations were performed for prefragment excitation energies* $E*$ *in the interval* [10,20] MeV *with a* 0.5 MeV *spacing.*

pass through, and they could largely be filtered by imposing another, higher, threshold energy.

5. Outlook and Conclusions

As of today, 2015-06-02, the CODEZ code is complete in the sense that it has models for all the quantities needed in a statistical decay code. However, there is a reason that the original, CODEX code had something close to seven models for everything: the code would be more accurate if it was used together with models suited for specific nuclei.

At this point, it should be fairly straightforward to implement new models. The object oriented structure of the code means that the user just has to inherit the approriate model object, and override the model they wish to change. To allow for the multiple models to coexist without forcing the user to recompile, it may be suitable to implement a *factory method* to declare which model class to use, and a corresponding new command-line option to control this factor method.

Since most of the functions accept a *Nucleus object* as input, the interface should have no problems to accomodate more general input parameters. For example: nuclei with a given deformation could be implemented by inheriting the nucleus class, and the same interface could be used for all these classes. There are some potential design problems with different models for deformation dependent parameters, since this places a burden on the models to implement functions for all kinds of deformation; the program may need to signal to the user when it cannot handle their nucleus subclass, so that it does not just run the undeformed case without the users knowledge. To some extent, it may be possible to place some of these burdens on the person implementing the nucleus subclasses, by forcing them to write functions to convert their deformation parametrization to a standardized one, but that may not be straightforward, especially if nuclei at the saddle-point for fission were to be implemented, with their rather distinct x-parameter shapes.

The current setup, with the simulation steps split into separate programs, should be very easy to run in parallel with something like GNU PARALLEL, but passing large amounts of data through a pipe may not be optimal from a performance point of view. At one point, it seemed as if performance would not be an issue, which motivated the decision to split up the program, but it may be worth to consider rewriting it with higher performance in mind. Although this structure has the advantage of having a standardized flow control (all sub-programs parse command-line options in much the same way), the long command lines required to run a specific tasks means that the user will want to keep it in a script, and it that point, they might as well have created an input file.

In short, there are a lot of things that could be done for the code. Whether the code

will actually do something for its users remains to be seen, and the curious reader is adviced to read the relevant appendices[1] on how to get started!

---

[1]To be implemented!

Bibliography

[1] GSI - R3B, 2014.
https://www.gsi.de/work/forschung/nustarenna/nustarenna_divisions/
kernreaktionen/activities/r3b.htm. (accessed 2015-04-16).

[2] J. Allison, K. Amako, J. Apostolakis, et al. Geant4 developments and applications.
IEEE Transactions on Nuclear Science, 53(1):270 –278, Feb. 2006.

[3] H. Johansson. ggland - command-line simulation wrapper, Apr 2013.
http://fy.chalmers.se/~f96hajo/ggland/.

[4] U. Gollerthan. Untersuchungen zur Emission geladener Teilchen bei der kalten
Fusion von ^{90}Zr $+$ ^{89}Y. Master's thesis, Technische Hochschule Darmstadt, 1988.

[5] M. D. Arjan Koning, Stéphane Hilaire. TALYS – A nuclear reaction program.
http://www.talys.eu/home/. (accessed 31 May 2015).

[6] J. J. Gaimard and K. H. Schmidt. A reexamination of the abrasion-ablation model
for the description of the nuclear fragmentation reaction. *Nuclear Physics A*, 531(3),
1991.

[7] J. Bowman, W. Swiatecki, and C. Tsang. *Abrasion and ablation of heavy ions.* Jul
1973. http://www.osti.gov/scitech/servlets/purl/4259977.

[8] N. Metropolis, R. Bivins, M. Storm, et al. Monte Carlo Calculations on In-
tranuclear Cascades. I. Low-Energy Studies. *Phys. Rev.*, 110:185–203, Apr 1958.
http://link.aps.org/doi/10.1103/PhysRev.110.185.

[9] F. Cucinotta, J. Wilson, J. Shinn, and R. Tripathi. Assessment and re-
quirements of nuclear reaction databases for {GCR} transport in the atmo-
sphere and structures. *Advances in Space Research*, 21(12):1753 – 1762, 1998.
http://www.sciencedirect.com/science/article/pii/S0273117798000623.

[10] A. Goldhaber. Statistical models of fragmentation pro-
cesses. *Physics Letters B*, 53(4):306 – 308, 1974.
http://www.sciencedirect.com/science/article/pii/0370269374903888.

[11] E. J. Moniz, I. Sick, R. R. Whitney, et al. Nuclear Fermi Momenta from
Quasielastic Electron Scattering. *Phys. Rev. Lett.*, 26:445–448, Feb 1971.
http://link.aps.org/doi/10.1103/PhysRevLett.26.445.

[12] K. H. Schmidt and W. Morawek. The conditions for the synthesis of heavy nuclei. *Reports on Progress in Physics*, 54(7), 1991.

[13] K. Krane. *Introductory Nuclear Physics*, chapter Nuclear Fission. Wiley, 1987.

[14] W. J. Swiatecki. NOTE ON NUCLEAR DISINTEGRATION WIDTHS. *Australian Journal of Physics*, 36(5):641–647, 1983.

[15] Wolfram Research, Inc. . Number of partitions of an integer into distinct parts: Introduction to partitions, 2015. http://functions.wolfram.com/IntegerFunctions/PartitionsQ/introductions/Partitions/ShowAll.html (accessed 2015-05-20).

[16] M. Grossjean and H. Feldmeier. Level density of a Fermi gas with pairing interactions. *Nuclear Physics A*, 444(1):113 – 132, 1985. http://www.sciencedirect.com/science/article/pii/0375947485902945.

[17] C. Goutis and G. Casella. Explaining the Saddlepoint Approximation. *The American Statistician*, 53(3):pp. 216–224, 1999. http://www.jstor.org/stable/2686100.

[18] International Atomic Energy Agency. *Handbook for calculations of nuclear reaction data, RIPL-2*, chapter Nuclear Level Densities. 2006.

[19] J. R. Grover. Shell-Model Calculations of the Lowest-Energy Nuclear Excited States of Very High Angular Momentum. *Phys. Rev.*, 157:832–847, May 1967. http://link.aps.org/doi/10.1103/PhysRev.157.832.

[20] T. Ericson. The statistical model and nuclear level densities. *Adv.Phys.*, 9:425–511, 1960.

[21] P. Moller, J. Nix, W. Myers, and W. Swiatecki. Nuclear Ground-State Masses and Deformations. *Atomic Data and Nuclear Data Tables*, 59(2):185 – 381, 1995. http://www.sciencedirect.com/science/article/pii/S0092640X85710029.

[22] J. Blocki, J. Randrup, W. Swiatecki, and C. Tsang. Proximity forces. *Annals of Physics*, 105(2):427 – 462, 1977. http://www.sciencedirect.com/science/article/pii/0003491677902494.

[23] C. D. Fosco, F. C. Lombardo, and F. D. Mazzitelli. An improved proximity force approximation for electrostatics. *Annals Phys.*, 327:2050–2059, 2012.

[24] C. D. Fosco, F. C. Lombardo, and F. D. Mazzitelli. The proximity force approximation for the Casimir energy as a derivative expansion. *Phys.Rev.*, D84:105031, 2011.

[25] I. Dutt and R. K. Puri. Comparison of different proximity potentials for asymmetric colliding nuclei. *Phys.Rev.*, C81:064609, 2010.

[26] M. Balasubramaniam and N. Arunachalam. Proton and α-radioactivity of spherical proton emitters. *Phys. Rev. C*, 71:014603, Jan 2005. http://link.aps.org/doi/10.1103/PhysRevC.71.014603.

[27] H. F. Zhang, Y. J. Wang, J. M. Dong, J. Q. Li, and W. Scheid. Concise methods for proton radioactivity. *Journal of Physics G: Nuclear and Particle Physics*, 37(8):085107–085107, 2010.

[28] W. D. Myers. Geometric properties of leptodermous distributions with applications to nuclei. *Nuclear Physics A*, 204(3):465 – 484, 1973. http://www.sciencedirect.com/science/article/pii/0375947473903886.

[29] J. M. Blatt and V. F. Weisskopf. *Theoretical Nuclear Physics*. Springer New York, New York, NY, 1979.

[30] E. C. Kemble. A Contribution to the Theory of the B. W. K. Method. *Phys. Rev.*, 48:549–561, Sep 1935. http://link.aps.org/doi/10.1103/PhysRev.48.549.

[31] C.-S. Ng. WKB - Not So Bad After All. *ArXiv e-prints*, June 2011.

[32] R. K. Adair. Nuclear Potential Well Depth. *Phys. Rev.*, 94:737–738, May 1954. `http://link.aps.org/doi/10.1103/PhysRev.94.737`.

[33] P. Chomaz. Collective excitations in nuclei. 1997.

[34] J. M. Moss, C. M. Rozsa, D. H. Youngblood, J. D. Bronson, and A. D. Bacher. Isoscalar Giant Resonance in Light Nuclei ($A < 40$). *Phys. Rev. Lett.*, 34:748–751, Mar 1975. http://link.aps.org/doi/10.1103/PhysRevLett.34.748.

[35] J. Speth. *Electric and Magnetic Giant Resonances in Nuclei*. International Review of Nuclear Physics Series. World Scientific Publishing Company Incorporated, 1991. https://books.google.se/books?id=o4423vnEoz8C.

[36] G. Audi. Experimental Chart of Nuclides 2000. `ie.lbl.gov/systematics/chart_qsp.pdf`. (accessed 31 May 2015).

[37] S. Lindberg. Optimised Use of Detector Systems for Relativistic Radioactive Beams. Master's thesis, Chalmers University of Technology, 2013.

A. Retrieving and running the CODEZ code

hj

B. Detailed documentation of the CODEZ code